FD-TD Synthesis and Resonance Based Identification of GPR returns from Buried Land-mines

W.R. van der Leij

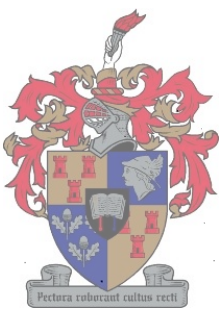

October 1999

Thesis presented in partial fulfilment
of the requirements for the degree of
Master of Science (Electronic Engineering)
at the
University of Stellenbosch

Supervisors: **Prof. D.B. Davidson** and **Prof. D.M. Weber**

Declaration

I, the undersigned, hereby declare that the work contained in this thesis is my own original work and has not previously in its entirety or in part been submitted at any university for a degree.

Date : November 22, 1999

Abstract

Numerical electro-magnetic methods are quickly gaining popularity in the design and optimisation of real world sensors that require complex and expensive testing. Most stepped-frequency GPRs synthesise a defined pulse in the time domain per frequency step. The FDTD method is well suited to modelling pulse propagation and computing scattering information from objects over a wide bandwidth.

The Body-of-Revolution expansion to the FDTD method reduces the dimensionality of the algorithm and significantly reduces the computation time and resource load of the simulations. The rotional symmetry requirement still allows the inclusion of a wide variety of land-mine target shapes and stratified media.

The BOR FDTD simulator is used to provide time domain data from buried scattering targets modelled to resemble real world conditions as closely as possible. Natural resonance information is extracted from this data using Linear Predictive Coding. Different land-mine targets will have different natural resonance signatures associated with them and these are used as feature vectors for the training and testing of artificial neural networks. Identification is then performed on a set of land-mines in the presence of ground cutter.

Opsomming

Numeriese elektro-magnetiese metodes raak toenemend gewild in die ontwerp en optimering van praktiese sensors wat komplekse en duur toetsing vereis. Meeste trap-frekwensie GPR sintetiseer 'n gedefinieerde puls in die tydgebied by elke frekwensiestap. Die FDTD metode is geskik vir die modulering van pulspropagasie en komputasie van veldverspreiding van objekte oor 'n wye bandwydte.

'n Liggaam-van-Omwenteling uitbreiding van die FDTD metode verminder die dimensionaliteit van die algoritme en dus beduidend die komputasietyd en geheue gebruik van die simulasie. Die rotasionele simmetrie vereiste laat nog die modulering van 'n wye stel landmyn teikens en gelaagde mediums toe.

Die BOR FDTD simulator word gebruik om tyd gebied gestrooide data vanaf landmyne te skep wat werêld kondisies so akkuraat as moontlik naboots. Liniêre voorspellende kodering word gebruik om natuurlike resonansie informasie uit die data te onttrek. Verskillende landmyn teikens het elkeen hul eie natuurlike resonansie beskrywing en dié kenmerkvektore word gebruik vir die ontwerp en validasie van neurale netwerke. Identifikasie op 'n stel landmyne in verskeie grond kondisies is gedoen.

Acknowledgements

Now unto him that is able to do exceeding abundantly above all that we ask or think, according to the power that worketh in us, unto him be glory in the church by Christ Jesus throughout all ages, world without end.

—

Ephesians 3:20,21

My greatest thanks and admiration go to my two advisors, Prof. D.B.Davidson and Prof. D.M.Weber. Their enthusiasm, insight and support for this project was more than I could have hoped for. It truly is a pleasure to work with people who know what they are talking about.

I'm especially blessed by and eternally thankful for my family and friends for their love and support through the past two years.

Charl, Carl, Jaco, Lude and Swannie. Together, they probably wrote more of my thesis than I did.

Carl and Goof, for ensuring that caffeine addiction was not an option but an eventuality.

To the rest of the research groups in the DSP and EM labs, there are few institutions which share the same level of encouragement and stimulation. Many thanks for an entertaining and educational two years.

Contents

List of Figures

List of Tables

Keywords

Body-of-Revolution, Finite-Difference Time-Domain, Ground Penetrating Radar, Land-Mine Detection

Acronyms

2-D	Two dimensional
3-D	Three dimensional
ABC	Absorbing Boundary Condition
AR	Auto-Regressive
BOR	Body of Revolution
FDTD	Finite-Difference Time-Domain
GPR	Ground-Penetrating Radar
LPC	Linear Predictive Coding
PML	Perfectly Matched Layer
RC	Reflection Coefficients
RCS	Radar Cross Section
RMS	Root Mean Square
SAR	Synthetic Aperture Radar
TE	Transverse Electric
TM	Transverse Magnetic

Notation

$\hat{x}$	Unit vector x
$\mathcal{O}$	Numerical computation operations
$\mathbf{F}^i$, $\mathbf{F}^s$, $\mathbf{F}^t$	Incident, Scattered or Total field component of vector field $\mathbf{F}$.
$z_n(kr) = \sqrt{\frac{\pi}{2kr}} Z_{n+1/2}(kr)$	Spherical Bessel functions
$\hat{Z}_n(kr) = krz_n(kr)$	Schulkenov spherical Bessel function
$P_n(\cos\theta)$	Ordinary Legendre functions
P_n^m	Associated Legendre functions

Chapter 1

Introduction

1.1 Overview

1.1.1 The Land-Mine Problem

In 1994 the U.S. State Department issued a report stating that there where over 110 million land-mines still to be cleared in the world. In Mozambique alone, the figures are largely quoted to be between 250 thousand and 1 million land-mines scattered across the country in over 1800 mine-fields. The statistics, albeit loose, express the need for urgent demining projects and innovative research initiatives. Buried mines in particular comprise the biggest problem to the demining effort.

1.1.2 The Detection Problem

The land-mines themselves vary in shape, size, composition, function and deployal technique. All of these factors are of importance from a detection point of view eg. deeply

buried mines pose a problem as a result of soil attenuation, plastic mines contain trace amounts of metal making detection with metal-detectors difficult and small mines are hard to resolve with sub-surface imaging techniques.

On the lowest level, the detector has to be able to distinguish between valid mine targets and common ground clutter. Foliage protection, climatic conditions and harsh terrain conditions complicate the matter further. Current detection techniques, in fact, rely heavily on these factors. Sniffer dogs have been employed as one of the most cost-effective and reliable techniques available, however, heat, wind and rain seriously hamper their performance. Infrared imaging techniques are too susceptible to foliage and temperature to be used effectively on their own. Ground-penetrating radar (GPR), however, is proving to be very promising prospective sensor platform being able to distinguish electro-magnetic returns from even plastic targets.

On a higher level, the detector should preferably be light-weight and therefore maneuverable to enable it to be used on most terrain. Cost is, as always, also a serious consideration. Lastly, an automated system that minimises the need for highly skilled operators is preferable [1].

1.2 Design Philosophy

GPR, as mentioned, is gaining popularity in research circles. Short-time pulses are used to obtain ultra-wideband time-domain data from the scattered fields reflected from buried objects. A growing number of GPR's, however, do operate in the frequency domain. This data is generally processed in one of two ways: if the C-scan data is available, synthetic aperture radar (SAR) inverse imaging techniques can be used with image recognition algo-

rithms [1], or, identification based on parameter estimation of the natural resonances of the target and its interaction with its surrounding medium can be applied.

The design of optimal automated detectors requires a large amount of training and testing data. The acquisition of real live GPR returns from land-mine targets can be an expensive, time consuming and, in most countries, a difficult task. The role and importance of computational electro-magnetic methods (CEM) thus comes to light in an initial development, design and optimisation phase [2]. Detection algorithms, clutter and ground effects and optimal sensor configurations can then be tested and designed *in principle*. If successful, this knowledge will be a motivating factor behind efforts to obtain real world data and will encourage further experimental development.

The goal here is to generate, as accurately as possible, large amounts of data that model GPR returns from a variety of ground conditions and land-mine targets. The emphasis will not placed on the representivity of the model, but rather on the *feasibility* of detecting land-mine targets embedded in a noisy environment.

1.3 Method

Bourgeois and Smith used the Finite-Difference Time-Domain (FDTD) method in the simulation of separated aperture sensors for mine detection [2]. The FDTD method finds its usefulness in this field in that it can accurately simulate wave propagation in both space and time. Wideband data is thus available from single excitations. Furthermore, it is possible to accurately describe complex scatterers throughout its computational domain.

It will be shown in chapter 2 that rotationally symmetric three dimensional (3-D) scattering

[1] This is used in fairly ideal soil conditions. Usually the inhomogenous nature of weathered soil surface destroys the phase information needed to construct the SAR image.

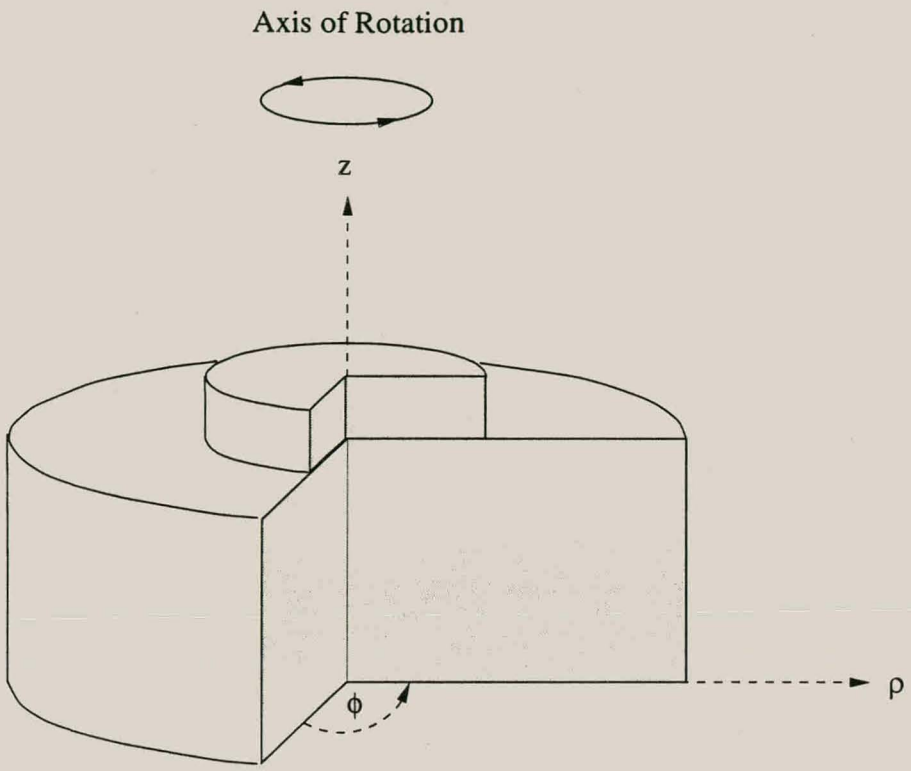

Figure 1.1: Rotationally Symmetric Object Model.

objects can, by a Fourier series expansion [3], be modelled as being two dimensional (2-D) (see figure 1.1). The result is that a computationally expensive 3-D FDTD algorithm can now be computed with a modified 2-D BOR FDTD algorithm requiring up to several orders of magnitude less computer memory and significantly quicker [4]. In fact, the formulation presented in chapter 3 (and validated in chapter 4) is able to compute on most high-end personal desktop computers and is suitable for parallelised implementation. The rotational symmetry requirement is not particularly restricting either. A large enough contingent of land-mines and cluttering objects can be modelled in this way [5] and stratified soil layers can be inserted with ease.

The BOR FDTD method is formulated and used to generate a time-domain data set of GPR returns off a number of mine and non-mine targets. The choice and modelling of these target classes is discussed in relative detail in chapter 5. In chapter 6, linear predictive

coding (LPC) is performed on each of the stored data sets to obtain the auto-regressive (AR) parameters. Reflection coefficients (RC's) are obtained from these AR parameters using the Levinson-Durbin recursive algorithm. The RC's so extracted are representative of the natural resonances present in the simulated GPR signal. This is a technique widely used in seismology [6] since the RC's are equivalent to the reflection coefficients of the physical media.

Class based detection using artificial neural networks (ANN) is then performed on these features, in chapter 7, to determine a *ball park* figure of detectability. This class based detection is performed on a *mine-no-mine* basis to obtain an idea of overall system performance. It is also performed on a *per class* basis to see exactly which classes are separable and by what degree. Lastly, it is performed on a selected set of targets that are found to be reasonably separable from the ground reflections and major clutter in order to investigate the effects of thermal receiver noise on the detectability of the model.

1.4 Contribution

This thesis describes the generation of simulated GPR data from buried land-mines in conditions approaching that of the real world at a greatly reduced computational cost than has been achieved before with a 3-D FDTD method. Furthermore, it puts forward a method of feature extraction based on system resonances for detection purposes. The multi-disciplinary nature of the thesis, combining CEM techniques with pattern recognition methods, is also a contribution. Lastly, the detectability of buried mine-like targets in stratified, lossy soil and noisy receiver environments is discussed.

Chapter 2

Body-of-Revolution Field Expansion

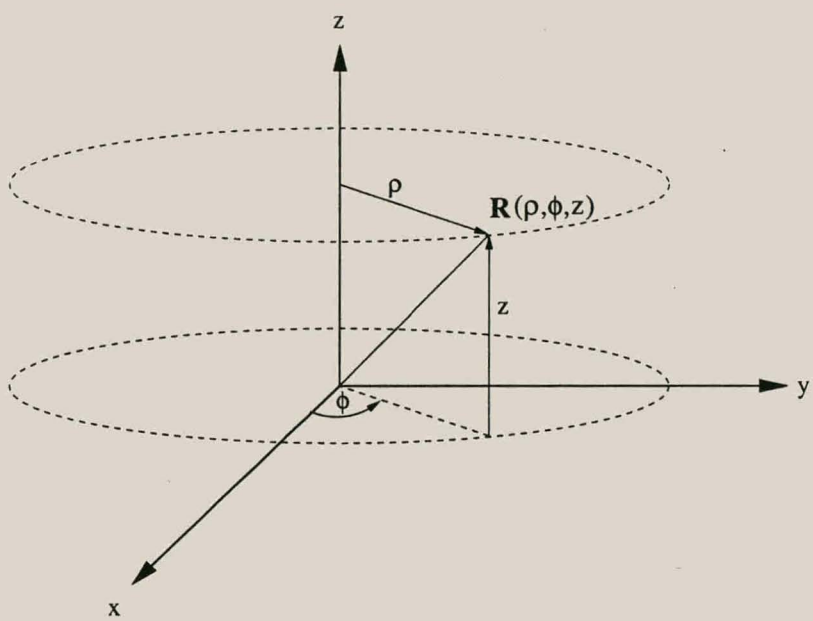

Figure 2.1: Body-of-Revolution Representation.

2.1 Introduction

The BOR formulation is structured around expanding the azimuthal field dependencies as an orthogonal Fourier series. This specific approach is based on Merewether and Fisher's report [3]. The objective is an electro-magnetic field description in cylindrical coordinates that is ϕ independent around the z-axis of rotation (figure 2.1). To complete the formulation, the curl operator for vector fields needs to be re-described in terms of the expanded Fourier modes.

2.2 Field Description

Assume an incident plane wave with propagation vector $\mathbf{k} = \mathbf{E} \times \mathbf{H}$ pointing towards the origin and lying in the $x - z$ plane (see figure 2.2). This can always be arranged given rotational symmetry.

We can express this vector in Cartesian coordinates as

$$\begin{aligned} \hat{k} &= \hat{x}\sin(-(\theta - \pi)) + \hat{z}\cos(-(\theta - \pi)) \\ &= \hat{x}\sin\theta - \hat{z}\cos\theta \end{aligned} \tag{2.1}$$

The incident electric-field vector at reference point $\mathbf{R} = \hat{\rho}\rho + \hat{z}z$ at time t is described as

$$\mathbf{E}^i = E\left(t - \frac{\hat{k}\cdot\mathbf{R}}{c}\right)(-\hat{y}\times\hat{k}) \tag{2.2}$$

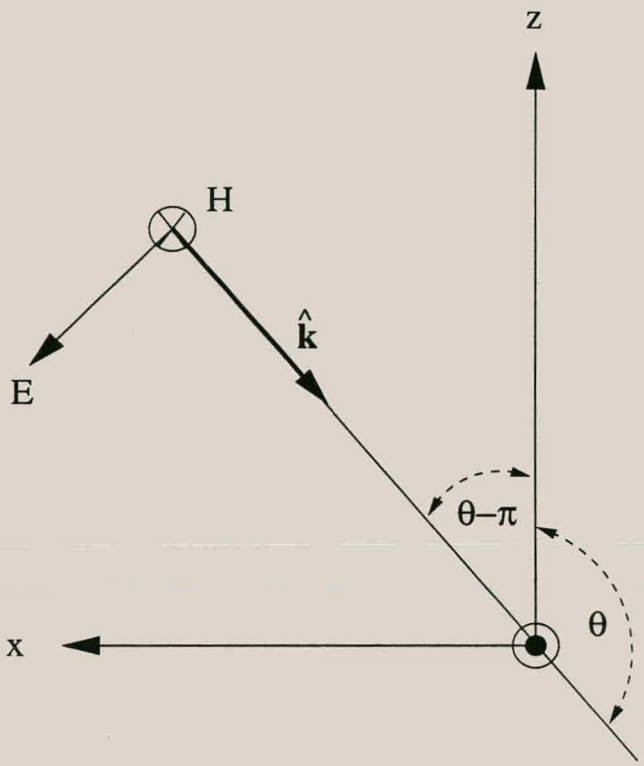

Figure 2.2: Plane Wave Propagation Vector **k** in the $x-z$ Plane.

where the cross product is defined as

$$-\hat{y}\times\hat{k}=\begin{vmatrix}\hat{x} & \hat{y} & \hat{z}\\ 0 & -1 & 0\\ \sin\theta & 0 & -\cos\theta\end{vmatrix}=\hat{x}\cos\theta+\hat{z}\sin\theta \tag{2.3}$$

Converting to the cylindrical coordinate system (see appendix A)

$$\begin{aligned}\hat{x} &= \hat{\rho}\cos\phi-\hat{\phi}\sin\phi \quad \text{and}\\ \hat{y} &= \hat{\rho}\cos\theta+\hat{\phi}\cos\phi\end{aligned}$$

results in

$$\mathbf{E}^i = E\left(t - \frac{\rho\sin\theta\cos\phi - z\cos\theta}{c}\right)(\hat{\rho}\cos\theta\cos\phi - \hat{\phi}\cos\theta\sin\phi + \hat{z}\sin\theta) \tag{2.4}$$

The incident magnetic-field vector at the same reference point $\mathbf{R}$ is perpendicular to the electric field (see figure 2.2) and is described as

$$\mathbf{H}^i = H\left(t - \frac{\hat{k}\cdot\mathbf{R}}{c}\right)(-\hat{\theta}\times\hat{k}) \tag{2.5}$$

where the cross product becomes the $-\hat{y}$ vector. Converting to cylindrical coordinates, the $\mathbf{H}^i$ field becomes

$$\mathbf{H}^i = H\left(t - \frac{\rho\sin\theta\cos\phi - z\cos\theta}{c}\right)(-\hat{\rho}\sin\phi - \hat{\phi}\cos\phi) \tag{2.6}$$

The ϕ component of the magnetic field is considered even with respect to angle ϕ while the ρ component is considered odd. The z component in this case is zero and can considered to be either even or odd. It is chosen as odd, in this formulation, for simplicity.

2.3 Fourier Series Expansion

Focusing on equations (2.4) and (2.6) the angular dependences of the electric and magnetic fields become apparent. The ρ and z components of the incident electric field and the ϕ component of the incident magnetic field are clearly even functions of ϕ and they can be expanded using a Fourier cosine series. From appendix B, the even field ($\mathbf{F}^e$) cosine expansion becomes

$$\mathbf{F}^e(\rho,\phi,z,t) = \frac{\mathbf{F}_0^e(\rho,z,t)}{2} + \sum_{k=1}^{\infty}\mathbf{F}_k^e(\rho,z,t)\cos(k\phi) \tag{2.7}$$

where

$$\mathbf{F}_0^e = \frac{2}{\pi}\int_0^{\pi} \mathbf{F}^e(\rho,\phi,z,t)d\phi \tag{2.8}$$

$$\mathbf{F}_k^e(\rho,z,t) = \frac{2}{\pi}\int_0^{\pi} \mathbf{F}^e(\rho,\phi,z,t)\cos(k\phi)d\phi \tag{2.9}$$

The ϕ component of the incident electric field and the ρ and z components of the magnetic field are odd functions of ϕ and can be expanded using a Fourier sine series. The odd field ($\mathbf{F}^o$) sine expansion becomes

$$\mathbf{F}^o(\rho,\phi,z,t) = \sum_{k=1}^{\infty} \mathbf{F}_k^o(\rho,z,t)\sin(k\phi) \tag{2.10}$$

where

$$\mathbf{F}_k^o(\rho,z,t) = \frac{2}{\pi}\int_0^{\pi} \mathbf{F}^o(\rho,\phi,z,t)\sin(k\phi)d\phi \tag{2.11}$$

The above expansions result in the analytical extraction of the azimuthal dependence of the $\mathbf{F}_o^e$, $\mathbf{F}_k^e$ and $\mathbf{F}_k^o$ terms.

2.4 The Curl Operator

For the cylindrical coordinate system, the curl operator on field $\mathbf{F}$ is defined as

$$\nabla\times\mathbf{F} = \left[\frac{1}{\rho}\frac{\partial F_z}{\partial\phi} - \frac{\partial F_\phi}{\partial z}\right]\hat{\rho} + \left[\frac{\partial F_\rho}{\partial z} - \frac{\partial F_z}{\partial\rho}\right]\hat{\phi} + \frac{1}{\rho}\left[\frac{\partial\rho F_\phi}{\partial\rho} - \frac{\partial F_\rho}{\partial\phi}\right]\hat{z} \tag{2.12}$$

The ϕ derivatives of the even and odd fields are determined analytically from equations (2.7) and (2.10) to be

$$\frac{\partial \mathbf{F}_e}{\partial \phi} = -\sum_{k=1}^{\infty} k\mathbf{F}_k^e(\rho, z, t)\sin(k\phi) \tag{2.13}$$

$$\frac{\partial \mathbf{F}_o}{\partial \phi} = \sum_{k=1}^{\infty} k\mathbf{F}_k^o(\rho, z, t)\cos(k\phi) \tag{2.14}$$

where the $\mathbf{F}_0^e(\rho, z, t)$ term is treated as constant with respect to ϕ.

The curl operator is expected to yield different results for the **E** and for the **H** fields. Looking at the $k = 0$ mode separately (and noting the even and odd ϕ dependencies derived in section 2.3)

$$\nabla \times \mathbf{E}_0 = \frac{1}{\rho}\frac{\partial E_{z0}}{\partial \phi}\hat{\rho} + \left[\frac{\partial E_{\rho 0}}{\partial z} - \frac{\partial E_{z0}}{\partial \rho}\right]\hat{\phi} - \frac{1}{\rho}\frac{\partial E_{\rho 0}}{\partial \phi}\hat{z} \tag{2.15}$$

$$\nabla \times \mathbf{H}_0 = -\frac{\partial H_{\phi 0}}{\partial z}\hat{\rho} + \frac{1}{\rho}\frac{\partial \rho H_{\phi 0}}{\partial \rho}\hat{z} \tag{2.16}$$

The $k \neq 0$ modes are given below for a single mode.

$$\nabla \times \mathbf{E}_k = \sin(k\phi)\left[\frac{-k}{\rho}E_{zk} - \frac{\partial E_{\phi k}}{\partial z}\right]\hat{\rho} + \cos(k\phi)\left[\frac{\partial E_{\rho k}}{\partial z} - \frac{\partial E_{zk}}{\partial \rho}\right]\hat{\phi} + \frac{\sin(k\phi)}{\rho}\left[\frac{\partial \rho E_{\phi k}}{\partial \rho} + kE_{\rho k}\right]\hat{z} \tag{2.17}$$

$$\nabla \times \mathbf{H}_k = \cos(k\phi)\left[\frac{k}{\rho}H_{zk} - \frac{\partial H_{\phi k}}{\partial z}\right]\hat{\rho} + \sin(k\phi)\left[\frac{\partial H_{\rho k}}{\partial z} - \frac{\partial H_{zk}}{\partial \rho}\right]\hat{\phi} + \frac{\cos(k\phi)}{\rho}\left[\frac{\partial \rho H_{\phi k}}{\partial \rho} - kH_{\rho k}\right]\hat{z} \tag{2.18}$$

2.5 Discussion

Equations (2.17) and (2.18) show that the azimuthal (ϕ) independence of the even and odd fields is preserved within the curl operator. This is expected from the linear super-position principle. The **E** and **H** fields are still positioned in three dimensional space, however, from equations (2.7) and (2.10), they need only be specified in terms of their ρ and z coordinates. The angular dependence is preserved in the modal expansion of the sine and cosine series, thus completing the BOR formulation.

Chapter 3

Finite-Difference Time-Domain Formulation

3.1 Introduction

The modelling of a GPR system requires data computed over a wide range of frequencies [7]. The FDTD method offers broadband responses for single excitations. Arbitrary three-dimensional objects are easily implementable and (for particular cases) a BOR expansion can be used to reduce the computational complexity of the simulator. The particular FDTD formulation in this chapter is designed for the modelling of rotationally symmetric:

- Lossy dielectrics,
- Magnetic materials and/or
- Isotropic materials.

The materials are further assumed to have frequency-independent constitutive parameters, although it is possible to extend the formulation for the inclusion of frequency-dispersive media [8, 9].

A BOR FDTD expansion in cylindrical coordinates (Chapter 2) was developed by Merewether and Fisher [3]. The same formulation is used here, following some minor typographical edits by Davidson and Ziolkowski [4]. The method is largely re-derived here for a few important purposes:

- for aiding in the explanation of the particular total-scattered field formulation developed in section 3.9
- for aiding in the depiction of the specific stencilling scheme described in section 3.6.
- the specific total-scattered field formulation used here enforces the incident electric field on the source plane.

The second point is important since the original sources are geared for implementation in FORTRAN which references arrays from element 1. The BOR FDTD simulator, presented in this dissertation, is coded in C++ which references its arrays from element zero. The correct consistent stencilling scheme is, therefore, of utmost importance.

3.2 Yee Algorithm

A method that directly solves Maxwell's equations in both space and time is required to describe the dynamic electro-magnetic field evolution.

$$\mu \frac{\partial \mathbf{H}}{\partial t} = -\nabla \times \mathbf{E} \tag{3.1}$$

$$\epsilon \frac{\partial \mathbf{E}}{\partial t} = \nabla \times \mathbf{H} - \mathbf{J} \tag{3.2}$$

Ampere (3.1) and Farady's (3.2) Differential Laws are expressed in an approximated form using a central differencing scheme :

$$\frac{\partial F}{\partial q} = \lim_{\Delta q \to 0} \frac{\Delta F}{\Delta q} = \frac{F\left(q + \frac{\Delta q}{2}\right) - F\left(q - \frac{\Delta q}{2}\right)}{\Delta q} \tag{3.3}$$

where F represents the field value and q the space or time quantity. This forms the backbone of the Finite Differencing method applied in section 3.5.

K.S Yee [10] introduced a method for interleaving the discretised **E** and **H** fields onto a space-time grid (see figure 3.1). The individual field components are mapped in a manner consistent with Ampere and Faraday's laws. These field components are updated successively in a leap-frog fashion, each cell requiring input only from its *nearest neighbour* in space and in time.

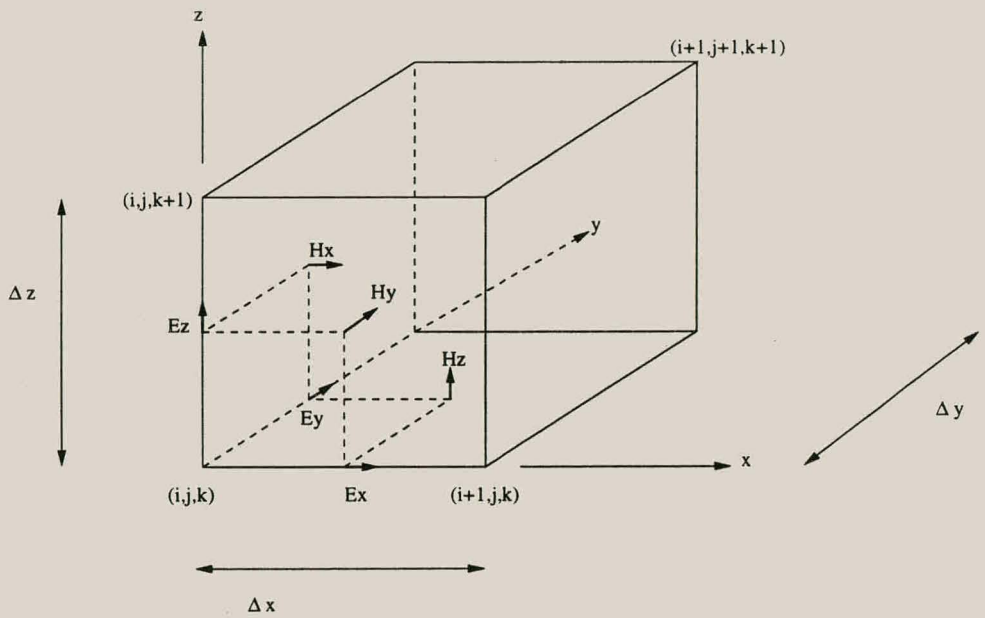

Figure 3.1: Yee Cell in 3-D.

3.3 On-axis Fourier Expansion

The Yee Algorithm was originally formulated for 3-D Cartesian coordinates. Following the Fourier series expansion described in chapter 2 and the curl operators expressed in (2.17-2.18), the Maxwell's equations (3.1-3.2) are expanded for each mode in cylindrical coordinates and are depicted in equations (3.4-3.9) for a single mode with and with the $\cos(k\phi)$ and $\sin(k\phi)$ terms suppressed.

$$-\mu\frac{\partial H_{\rho k}}{\partial t} = \left[\frac{-k}{\rho}E_{zk} - \frac{\partial E_{\phi k}}{\partial z}\right] \tag{3.4}$$

$$-\mu\frac{\partial H_{\phi k}}{\partial t} = \left[\frac{\partial E_{\rho k}}{\partial z} - \frac{\partial E_{zk}}{\partial \rho}\right] \tag{3.5}$$

$$-\mu\frac{\partial H_{zk}}{\partial t} = \frac{1}{\rho}\left[\frac{\partial(\rho E_{\phi k})}{\partial \rho} + kE_{\rho k}\right] \tag{3.6}$$

$$\epsilon\frac{\partial E_{\rho k}}{\partial t} + \sigma E_{\rho k} = \left[\frac{k}{\rho}H_{zk} - \frac{\partial H_{\phi k}}{\partial z}\right] \tag{3.7}$$

$$\epsilon\frac{\partial E_{\phi k}}{\partial t} + \sigma E_{\phi k} = \left[\frac{\partial H_{\rho k}}{\partial z} - \frac{\partial H_{zk}}{\partial \rho}\right] \tag{3.8}$$

$$\epsilon\frac{\partial E_{zk}}{\partial t} + \sigma E_{zk} = \frac{1}{\rho}\left[\frac{\partial(\rho H_{\phi k})}{\partial \rho} - kH_{\rho k}\right] \tag{3.9}$$

With the incident transverse electro-magnetic (TEM) field directed along the axis of rotation (z-axis), only the $k = 1$ mode is non-zero [4]. This assumption justifies the use of the Fourier expansion since the problem space is effectively reduced to two dimensions with only a single mode required in the solution (separate FDTD problems would have to be solved for any higher-order modes present).

3.4 Computational Requirements

It is generally accepted that as the electromagnetic size of structure increases, so does the required number of samples per wavelength to avoid grid dispersion errors. To model a 3-D volume of size L^3 over $N \propto L$ time steps, the grid space grows with $((L/\Delta L)^{1.5})^3$ (the 1.5 exponent is to control dispersion across the grid.) The run time of a 3-D FDTD code generally is of the order of $\mathcal{O}\left((L/\Delta L)^{1.5}\right)^3 \times N = \mathcal{O}(L/\Delta L)^{5.5}$ computations [4]. For systems larger than a few wavelengths, the computational power necessary becomes immense as the number of computations grows to the fourth power of the number of dimensions. The BOR approach reduces the system complexity by one dimension. What would have cost $\mathcal{O}(L/\Delta L)^{5.5}$ computations now only costs $\mathcal{O}(L/\Delta L)^4$. Long running simulations can thus be reduced in time by more than an order of magnitude as opposed to the 3-D FDTD simulations, making it a very attractive option.

3.5 Finite Difference Equations

Equations (3.4-3.9) are discretised using a second-order central differencing scheme (3.3).

$$\frac{\mu(\rho,z)}{\Delta t}\left[H_\rho\left(\rho,z,t+\frac{\Delta t}{2}\right)-H_\rho\left(\rho,z,t-\frac{\Delta t}{2}\right)\right] = \frac{1}{\rho}E_z(\rho,z,t) + \frac{1}{\Delta z}\left[E_\phi\left(\rho,z+\frac{\Delta z}{2},t\right)-E_\phi\left(\rho,z-\frac{\Delta z}{2},t\right)\right] \quad (3.10)$$

$$\frac{\mu(\rho,z)}{\Delta t}\left[H_\phi\left(\rho,z,t+\frac{\Delta t}{2}\right)-H_\phi\left(\rho,z,t-\frac{\Delta t}{2}\right)\right] = \frac{1}{\Delta\rho}\left[E_z\left(\rho+\frac{\Delta\rho}{2},z,t\right)-E_z\left(\rho-\frac{\Delta\rho}{2},z,t\right)\right] - \frac{1}{\Delta z}\left[E\rho\left(\rho,z+\frac{\Delta z}{2},t\right)-E_\rho\left(\rho,z-\frac{\Delta z}{2},t\right)\right] \quad (3.11)$$

$$\frac{\mu(\rho,z)}{\Delta t}\left[H_z\left(\rho,z,t+\frac{\Delta t}{2}\right)-H_z\left(\rho,z,t-\frac{\Delta t}{2}\right)\right] = -\frac{1}{\Delta\rho}E_\rho(\rho,z,t) - \frac{1}{\rho\Delta\rho}\left[\left(\rho+\frac{\Delta\rho}{2}\right)E_\phi\left(\rho+\frac{\Delta\rho}{2},z,t\right) - \left(\rho-\frac{\Delta\rho}{2}\right)E_\phi\left(\rho-\frac{\Delta\rho}{2},z,t\right)\right] \quad (3.12)$$

$$\frac{\epsilon(\rho,z)}{\Delta t}\left[E_\rho\left(\rho,z,t+\frac{\Delta t}{2}\right)-E_\rho\left(\rho,z,t-\frac{\Delta t}{2}\right)\right] + \sigma(\rho,z)E_\rho(\rho,z,t) = \frac{H_z(\rho,z,t)}{\Delta\rho} - \frac{1}{\Delta z}\left[H_\phi\left(\rho,z+\frac{\Delta z}{2},t\right)-H_\phi\left(\rho,z-\frac{\Delta z}{2},t\right)\right] \quad (3.13)$$

$$\frac{\epsilon(\rho,z)}{\Delta t}\left[E_\phi\left(\rho,z,t+\frac{\Delta t}{2}\right)-E_\phi\left(\rho,z,t-\frac{\Delta t}{2}\right)\right] + \sigma(\rho,z)E_\phi(\rho,z,t) = \frac{1}{\Delta z}\left[H_\rho\left(\rho,z+\frac{\Delta z}{2},t\right)-H_\rho\left(\rho,z-\frac{\Delta z}{2},t\right)\right] - \frac{1}{\Delta\rho}\left[H_z\left(\rho+\frac{\Delta\rho}{2},z,t\right)-H_z\left(\rho-\frac{\Delta\rho}{2},z,t\right)\right] \quad (3.14)$$

$$\frac{\epsilon(\rho,z)}{\Delta t}\left[E_z\left(\rho,z,t+\frac{\Delta t}{2}\right)-E_z\left(\rho,z,t-\frac{\Delta t}{2}\right)\right] + \sigma(\rho,z)E_z(\rho,z,t) = \frac{1}{\rho\Delta\rho}\left[\left(\rho+\frac{\Delta\rho}{2}\right)H_\phi\left(\rho+\frac{\Delta\rho}{2},z,t\right)-\left(\rho-\frac{\Delta\rho}{2}\right)H_\phi\left(\rho-\frac{\Delta\rho}{2},z,t\right)\right] - \frac{H_\rho(\rho,z,t)}{\rho} \quad (3.15)$$

The above equations give insight into why BOR is often referred to as being 2.5 dimensional. The grid-space is reduced to two dimensions with the omission of the $\frac{\partial}{\partial \phi}$ operator, but all six three-dimensional field components are still evaluated.

The Maxwell's equations expressed in this form show that each *new* field component in time is determined solely from the *nearest* field points determined previously in time.

3.6 Consistent Stencil Scheme

A stencil scheme needs to be chosen for the given field component topology which will aid in efficient implementation of the FDTD code. A modified Yee cell (figure 3.2) is used for referencing the field components in time and space. In this way a *template* can be set up that will ensure consistency. Equations (3.10-3.15) show that by choosing a starting point (the origin) and updating the field differentials in a leap-frog manner, the field behaviour can be marched forward in time and space.

The physical problem space is divided into $i_{max} \times j_{max}$ cells, each of which are $\Delta\rho \times \Delta z\ m^2$. First the magnetic fields are updated and then the electric fields since each relies on previous values of the other. The choice of starting point is arbitrary but consistency from this choice is essential. The process is run n_{max} times corresponding to a simulation time of $t = n_{max}\Delta t\ s$.

The σ terms in equations (3.13-3.15) introduce a problem in maintaining time consistency with the electric field updates. This is overcome by time averaging the electric field components of these terms over one time step as follows:

$$\sigma(\rho, z)E(\rho, z, t) = \sigma(\rho, z)\frac{E(\rho, z, t + \Delta t/2) - E(\rho, z, t - \Delta t/2)}{2} \tag{3.16}$$

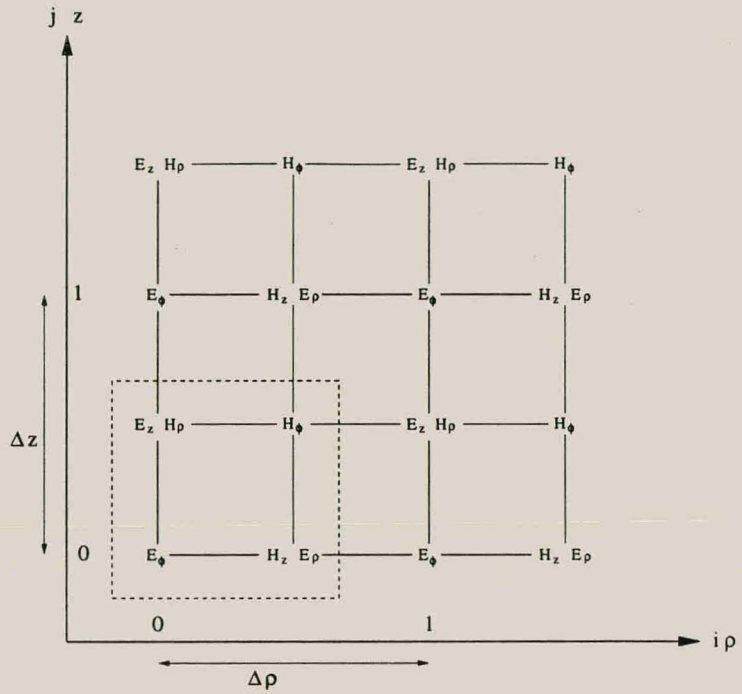

Figure 3.2: Modified Yee Cell in 2-D.

The like terms can then be grouped together.

The modified Yee cell (figure 3.2) aids in choosing indexes for updating the field update equations. A reasonable starting point is to place the ϕ component of the electric field at the origin of the stencil and to begin the updating from there. The field update equations can then be expressed as below, where the subscript of each field component refers to its spatial position and the superscript refers to the temporal update value.

$$H_\rho^{n+1}(i,j) = H_\rho^n(i,j) + \frac{\Delta t}{\mu(i,j)}\left[\frac{E_z^n(i,j)}{i}\right] + \frac{\Delta t}{\mu(i,j)}\left[\frac{E_\phi^n(i,j+1) - E_\phi^n(i,j)}{\Delta z}\right] \quad (3.17)$$

$$H_\phi^{n+1}(i,j) = H_\phi^n(i,j) - \frac{\Delta t}{\mu(i,j)}\left[\frac{E_\rho^n(i,j+1) - E_\rho^n(i,j)}{\Delta z}\right] + \frac{\Delta t}{\mu(i,j)}\left[\frac{E_z^n(i+1,j) - E_z^n(i,j)}{\Delta \rho}\right] \quad (3.18)$$

$$H_z^{n+1}(i,j) = H_z^n(i,j) - \frac{\Delta t}{\mu(i,j)}\left[\frac{(i+1)E_\phi^n(i+1,j) - iE_\phi^n(i,j)}{(i+1/2)\Delta \rho}\right] - \frac{\Delta t}{\mu(i,j)}\left[\frac{E_\rho^n(i,j)}{(i+1/2)}\right] \quad (3.19)$$

$$B(i,j+1)E_\rho^{n+1}(i,j+1) = A(i,j+1)E_\rho^n(i,j+1) + \frac{H_z^{n+1}(i,j+1)}{(i+1/2)} - \frac{H_\phi^{n+1}(i,j+1) - H_\phi^{n+1}(i,j)}{\Delta z} \quad (3.20)$$

$$B(i+1,j+1)E_\phi^{n+1}(i+1,j+1) = A(i+1,j+1)E_\phi^n(i+1,j+1) + \frac{H_\rho^{n+1}(i+1,j+1) - H_\rho^{n+1}(i+1,j)}{\Delta z} - \frac{H_z^{n+1}(i+1,j+1) - H_z^{n+1}(i,j+1)}{\Delta \rho} \quad (3.21)$$

$$B(i+1,j)E_z^{n+1}(i+1,j) = A(i+1,j)E_z^n(i+1,j) + \frac{(i+3/2)H_\phi^{n+1}(i+1,j) - (i+1/2)H_\phi^{n+1}(i,j)}{(i+1)\Delta \rho} - \frac{H_\rho^{n+1}(i+1,j)}{(i+1)} \quad (3.22)$$

where

$$A(i,j) = \frac{\epsilon(i,j)}{\Delta t} - \frac{\sigma(i,j)}{2} \tag{3.23}$$

$$B(i,j) = \frac{\epsilon(i,j)}{\Delta t} + \frac{\sigma(i,j)}{2} \tag{3.24}$$

The initial condition is to assume that all the fields are zero for $t \leq 0$. The **H** fields are updated first and then the **E** fields in the leap-frog manner described above.

3.7 Material Parameters

The problem space is comprised of an orthogonal grid of cells. Scattering objects and propagating media built into the problem space can, however, introduce staircase approximation errors, especially at angles normal to oblique sides of the scatterer (figure 3.3). [1] Kunz and Leubbers [11] suggest averaging across the interfaces between the mediums, to

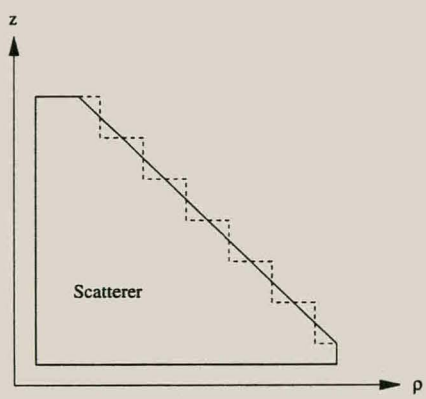

Figure 3.3: Staircase Approximation Error.

reduce any far field errors introduced by these staircase approximations. Another option

[1] The BOR expansion introduces a cylindrical gridding scheme, so no such approximation error will be made in the ρ = constant plane.

is to introduce a non-orthogonal grid scheme in problem areas. Both these options will increase the complexity of the simulator and, possibly, the run-time. For electrically large scatterers (order of a wavelength), the cells are considered small enough, compared to the dimensions of the scatterer, that such staircase quantisation effects are assumed negligible.

The previous section shows that the dielectric parameters and the conductivity of the mediums throughout the problem space can be specified explicitly. Some care has to be taken though, to ensure that they are set consistently with the modified Yee cell (figure 3.2). In other words, grids are set up for the ϵ, μ and σ parameters throughout the problem space in exactly the same manner as for the field quantities.

3.8 Stability

The FDTD formulation employs spatial and temporal discretisation in evaluating the Maxwell's equations numerically. Certain stability requirements exist to ensure that numerical dispersion is minimised and that aliasing is avoided.

The spatial step size should be small enough to model the finer geometrical details. The Nyquist sampling theorem requires discretising less than half the wavelength for the specific medium. However, to reduce numerical dispersion errors introduced by the higher frequencies of the waveform (the pulse being wideband), the spatial step size needs to be considerably less. A quoted *rule of thumb* is traditionally accepted as being no less than 10 samples per wavelength [12], however, this is a weak condition and for more accurate results, *at least* 25 samples per shortest wavelength should be taken.

The Courant-Friederichs-Levy [13] criterion is used to ensure that the computational velocity (the *velocity* at which the updates occur in space) is greater than the wave velocity

for the medium. The upper limit on the temporal step size becomes

$$\Delta t \leq \frac{1}{v_{max}} \left[\frac{(k+1)^2 + 2.8}{4\Delta\rho^2} + \frac{1}{\Delta z^2} \right]^{-1/2} \tag{3.25}$$

v_{max} is the highest wave-speed in the problem space. With Fourier mode $k = 1$ and $\Delta z = \Delta\rho = \Delta$, the above relation reduces to $\Delta t \leq \Delta/(v_{max}\sqrt{2.7})$.

The temporal discretisation can also be neatly described in terms of the 2-D Courant limit below for the $k = 1$ mode

$$\Delta t = \frac{\zeta\Delta}{v_{max}\sqrt{2}} = \zeta\Delta t_{2-D} \tag{3.26}$$

where $\zeta \leq 0.86$ is the Courant variable.

3.9 Total-Scattered Field Formulation

Maxwell's equations (3.1-3.2) can be decomposed linearly from total electric and magnetic fields into the superposition of incident fields $(\mathbf{E}^i, \mathbf{H}^i)$ and scattered fields $(\mathbf{E}^s, \mathbf{H}^s)$. The incident fields are known *a priori* at all points of the problem space and would be the field values that exist in the absence of any scatterers. The scattered fields result from the interaction of the incident wave and any materials in the grid. The finite difference approximations to the Yee algorithm can be applied with equal validity to any of the incident, scattered or total field vector components.

Kunz and Leubbers [11] present a pure scattered field FDTD formulation in which only the scattered fields are determined within the problem space. The incident fields are superimposed along their source boundaries. This formulation is based on the premise that the scattered fields are more readily absorbed by outer radiating boundary conditions. Hol-

land and Williams [14] determined that a total field FDTD formulation (in which the total fields are determined within the problem space) is superior to a pure scattered field FDTD formulation in terms of numerical dispersion considerations.

The total-scattered field FDTD formulation is a hybrid between the two methods. The problem space is divided into two regions: a total field region containing the scattering materials; and a scattered field region in which there is no incident field present. The two regions are separated by a non-physical interface (the source plane) which serves to 'inject' the incident wave into the total field region. This makes the total-scattered field FDTD formulation very apt for simulating plane wave illumination [15]. Figure 3.4 shows how the problem space is set up for the BOR formulation.

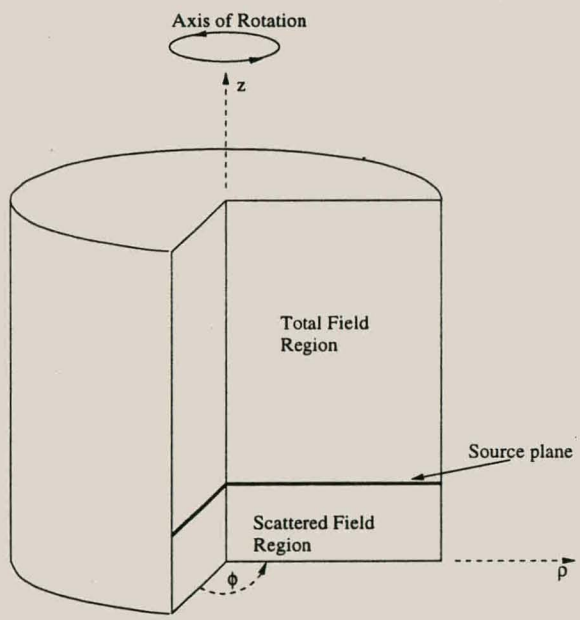

Figure 3.4: Total-Scattered Field Formulation in Cylindrical Coordinates.

3.9.1 Incident Uniform Plane Wave Illumination

The incident wave is assumed propagating along the z axis in the form described in equation (2.2).

$$\mathbf{E}^i = f(x, y)E(t - z/c)\hat{x} \tag{3.27}$$

c is the free-space wave speed and $f(x, y)$ is a spatial weighting factor. The above can be expressed in cylindrical coordinates as

$$\mathbf{E}^i = f(\rho)E(t - z/c)[\cos(\phi)\hat{\rho} - \sin(\phi)\hat{\phi}] \tag{3.28}$$

The above equation also shows why only the $k = 1$ mode is non-zero.

Figure 3.4 shows the source plane on the boundary between the total and scattered field regions upon which the incident wave is imposed. The field will radiate outward with a fixed transverse dependence. A Gaussian beam model is used to describe the field's spatial weighting in order to model typical wave propagation behaviour [16].

$$f(\rho) = e^{-(\rho/W)^2} \tag{3.29}$$

W is the $1/e$ amplitude on the Gaussian curve (figure 3.5). This source model is the simplest to implement without having to physically insert an antenna configuration into the problem space.

3.9.2 Implementation

The source plane is chosen as depicted in figure 3.6. This choice is arbitrary, however, in the vicinity of the interface plane, the update equations (3.17 - 3.22) need to be modified

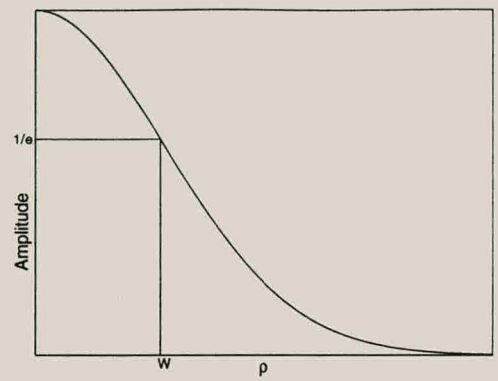

Figure 3.5: Incident Field Spatial Weighting.

to ensure that the fields in the total and scattered field regions evolve correctly. This modification involves either adding the incident fields on the interface plane (to obtain the total fields) or subtracting it just before (to ensure the total fields do not propagate into the scattered field region). The incident fields are transversely polarised and therefore contain only tangential components [2] to the constant z interface plane.

The **H** fields are updated first (section 3.6) and require knowledge of the $\mathbf{E}^i$ at the source plane. The **E** fields are updated a half time step ($\Delta t/2$) later and require knowledge of the $\mathbf{H}^i$ fields at the source plane. Figure 3.6 shows how consistency is maintained on a per-component basis. In the vicinity of the source plane (j_{src}), the update equations (before modification) contain a mixture of both total and scattered field components [4] as below:

$$H_\rho^{n+1}(i, j_{\text{src}}) = H_\rho^{s,n}(i, j_{\text{src}}) + \frac{\Delta t}{\mu(i, j_{\text{src}})} \left[\frac{E_z^{s,n}(i, j_{\text{src}})}{i} + \frac{E_\phi^{t,n}(i, j_{\text{src}} + 1) - E_\phi^{s,n}(i, j_{\text{src}})}{\Delta z} \right] \quad (3.30)$$

[2] In this case only ρ and ϕ components.

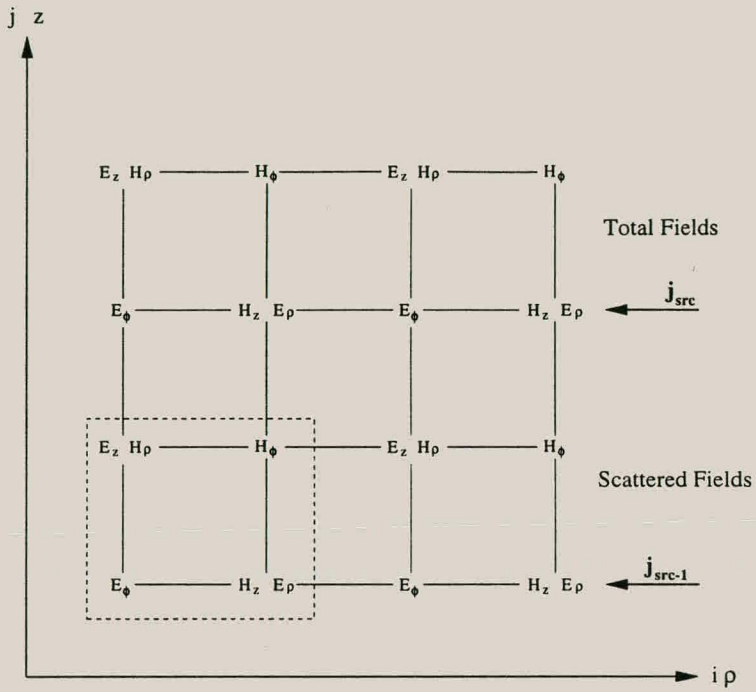

Figure 3.6: Source Plane in Modified Yee Cell.

$$H_{\phi}^{n+1}(i,j_{\text{src}}) = H_{\phi}^{s,n}(i,j_{\text{src}}) - \frac{\Delta t}{\mu(i,j_{\text{src}})}\left[\frac{E_{\rho}^{t,n}(i,j_{\text{src}}+1) - E_{\rho}^{s,n}(i,j_{\text{src}})}{\Delta z}\right] + \frac{\Delta t}{\mu(i,j_{\text{src}})}\left[\frac{E_{z}^{s,n}(i+1,j_{\text{src}}) - E_{z}^{s,n}(i,j_{\text{src}})}{\Delta \rho}\right] \quad (3.31)$$

$$B(i,j_{\text{src}}+1)E_{\rho}^{n+1}(i,j_{\text{src}}+1) = A(i,j_{\text{src}}+1)E_{\rho}^{t,n}(i,j_{\text{src}}+1) + \frac{H_{z}^{t,n}(i,j_{\text{src}}+1)}{(i+1/2)} - \frac{H_{\phi}^{t,n}(i,j_{\text{src}}+1) - H_{\phi}^{s,n}(i,j_{\text{src}})}{\Delta z} \quad (3.32)$$

$$B(i+1,j_{\text{src}}+1)E_{\phi}^{n+1}(i+1,j_{\text{src}}+1) = A(i+1,j_{\text{src}}+1)E_{\phi}^{t,n}(i+1,j_{\text{src}}+1) + \frac{H_{\rho}^{t,n}(i+1,j_{\text{src}}+1) - H_{\rho}^{s,n}(i+1,j_{\text{src}})}{\Delta z} - \frac{H_{z}^{t,n}(i+1,j_{\text{src}}+1) - H_{z}^{t,n}(i,j_{\text{src}}+1)}{\Delta \rho} \quad (3.33)$$

The H_ρ update equation needs to be modified by subtracting an incident field component from the total field term in order to ensure that only the scattered fields are updated.

$$H_\rho^s(i, j_{\text{src}}) = H_\rho(i, j_{\text{src}}) - \frac{\Delta t}{\mu(i, j_{\text{src}})\Delta z} E_\phi^i(i, j_{\text{src}} + 1) \tag{3.34}$$

Similarly, the H_ϕ update equation needs to have an incident field term added to ensure that only scattered field terms are updated.

$$H_\phi^s(i, j_{\text{src}}) = H_\phi(i, j_{\text{src}}) + \frac{\Delta t}{\mu(i, j_{\text{src}})\Delta z} E_\rho^i(i, j_{\text{src}} + 1) \tag{3.35}$$

The electric fields, from figure 3.6 are updated as total fields. The E_ρ component needs to have an incident field term added to ensure consistency.

$$B(i, j_{\text{src}} + 1)E_\rho^t(i, j_{\text{src}} + 1) = B(i, j_{\text{src}} + 1)E_\rho(i, j_{\text{src}} + 1) + \frac{1}{\Delta z} H_\phi^i(i, j_{\text{src}}) \tag{3.36}$$

Lastly, the E_ϕ component is modified by subtracting an incident field term.

$$B(i+1, j_{\text{src}} + 1)E_\phi(i+1, j_{\text{src}} + 1) = B(i+1, j_{\text{src}} + 1)E_\phi^t(i+1, j_{\text{src}} + 1) - \frac{1}{\Delta z} H_\rho^i(i+1, j_{\text{src}}) \tag{3.37}$$

From the above equations and discussion, the $\mathbf{H}^i$ fields are updated $-\Delta t/2$ behind the $\mathbf{E}^i$ fields. They are also applied to field components $-\Delta z/2$ cells before, so the propagation time over this half spatial step needs to be considered. The total time retardation (t_r) between the $\mathbf{E}^i$ and $\mathbf{H}^i$ fields therefore becomes

$$t_r = -\frac{\Delta z}{2c} - \frac{\Delta t}{2} \tag{3.38}$$

where the free-space wave speed (c) is used as it is presumed that the GPR housing lies above the ground.

3.10 Absorbing Boundary Conditions

The FDTD domain is of a finite size. The edges of the domain will introduce reflections and unpredictable behaviour unless care is taken to ensure that proper wave propagation is enforced over the outer boundaries. The inner *wall* at $\rho = 0$ corresponds to the axis of rotation. The tangential electric fields are set to zero on this boundary in order to enforce a perfect electric conductor (PEC).

$$\mathbf{E}_{\substack{\tan \\ \rho=0}} = 0 \quad \therefore E_{\substack{\phi \\ \rho=0}} = E_{\substack{z \\ \rho=0}} = 0 \tag{3.39}$$

The Berenger Perfectly Matched Layer (PML) is quickly gaining popularity as it offers $> 40dB$ absorption, is frequency independent and is independent of incidence angle [17]. A PML implementation for BOR coordinate systems using complex stretched coordinates is presented in appendix D. It is shown there that the update equations used in solving for the PML region display a radial dependence and that the complexity of the formulation increases dramatically, especially when dealing with lossy materials. Unfortunately, little work has been done to date on efficient optimisation of the PML for arbitrary BOR arrangements.

An alternate ABC based on the one-way wave equation is used instead for simplicity. The FDTD domain is made large enough to incorporate the Gaussian incident beam, therefore, ABC's that are valid for near-grazing incidence on the side boundary ($\rho = \rho_{max}$) of the problem space are not necessary. The top ($z = 0$) and bottom ($z = z_{max}$) boundaries as well as the side boundary ($\rho = \rho_{max}$) are treated with an ABC. The one-way wave equation is expressed as (for a z directed wave)

$$\left[\frac{\partial}{\partial z} \mp \frac{1}{v}\frac{\partial}{\partial t}\right] \phi(z,t) = 0 \tag{3.40}$$

where $\phi(z,t)$ is the field quantity and v is the wave speed in the medium at the boundary. The derivation of the procedure is given in appendix C. The ABC's are applied to the

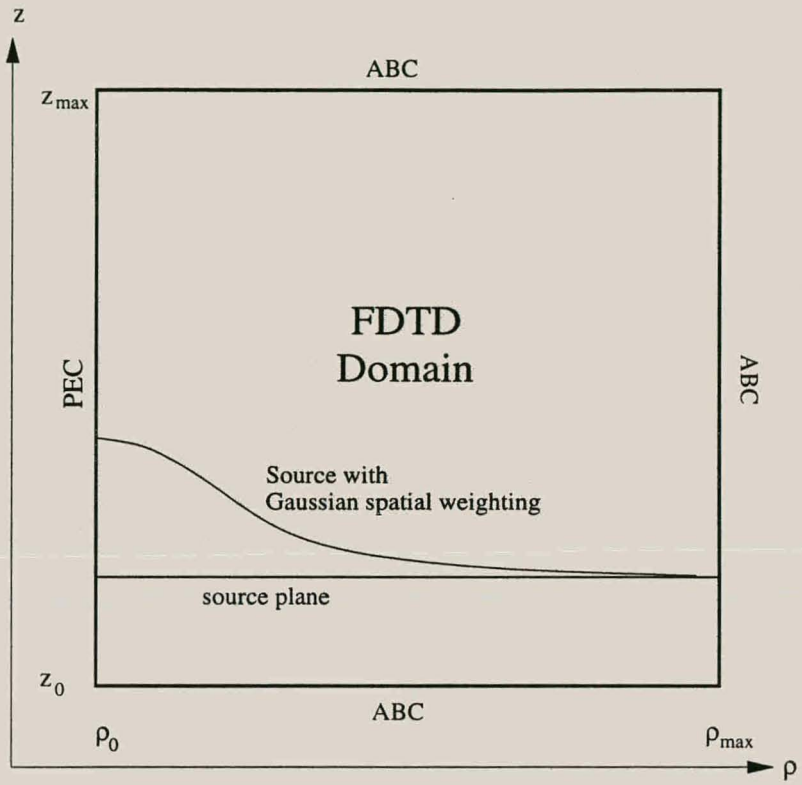

Figure 3.7: ABC Placement.

tangential **E** fields for each boundary.

The $z = 0$ boundary assumes an incident wave travelling in the $-z$ direction. The ABC update equations here are determined from equation(C.3).

$$E^{n+1}_{\rho,\phi}(i,0) = E^{n}_{\rho,\phi}(i,0)\left[\frac{1-c\Delta t}{\Delta z}\right] + E^{n}_{\rho,\phi}(i,1)\frac{c\Delta t}{\Delta z} \tag{3.41}$$

Notice that the free-space wave speed is used as it is assumed that the $z = 0$ boundary lies above the ground.

The $z = z_{max}$ boundary assumes an incident wave travelling in the $+z$ direction. The ABC

update equations here are determined from equation (C.4).

$$E_{\rho,\phi}^{n+1}(i, j_{max}) = E_{\rho,\phi}^{n}(i, j_{max}) \left[\frac{1 - v(i, j_{max})\Delta t}{\Delta z}\right] + E_{\rho,\phi}^{n}(i, j_{max} - 1)\frac{v(i, j_{max})\Delta t}{\Delta z} \quad (3.42)$$

The wave speed v is given a spatial reference in the event of the presence of more than one different propagating media.

Lastly, the $\rho = \rho_{max}$ boundary is treated very similarly to the $z = z_{max}$ boundary. Here the incident wave is assumed to be travelling in the $+\rho$ direction and the ABC update is determined from equation (C.6).

$$E_{\phi,z}^{n+1}(i_{max}, j) = E_{\phi,z}^{n}(i_{max}, j) \left[\frac{1 - v(i_{max}, j)\Delta t}{\Delta \rho}\right] + E_{\phi,z}^{n}(i_{max} - 1, j)\frac{v(i_{max}, j)\Delta t}{\Delta \rho} \quad (3.43)$$

Chapter 4

Validation

4.1 Introduction

Before generating the GPR scattering data set, the BOR FDTD simulator will be compared to known analytical solutions in this chapter. Four cases are considered:

1. The wave speed within dielectric and magnetic media is extracted.
2. Normally incident reflection and transmission coefficients off dielectric and magnetic layers are computed and compared to theory.
3. The scattering by a conducting sphere is compared to a known analytical solution.
4. The scattering by a dielectric sphere is compared to a similar analytic solution.

4.2 Incident Field Waveform

The incident pulse waveform used in the BOR FDTD simulator for all the test cases presented in this chapter is a sine modulated Gaussian pulse defined as

$$f(t) = \sin(2\pi f_c t) * \exp\left\{-\left[\left(\frac{10}{\tau}\right)(t - \tau/3)\right]^2\right\} \tag{4.1}$$

where $f_c = 1\text{GHz}$ is the centre frequency of the pulse which corresponds to a free-space wavelength of 30cm. $\tau = 3/F_c$ is the pulse duration (set to three wavelengths). Figures 4.1 and 4.2 depict the pulse waveform in the time and frequency domains respectively. This pulse was chosen for its zero DC value and smooth turn-on and turn-off characteristics. From figure 4.2, the -10db bandwidth of the pulse lies between 230MHz and 2.2GHz. This bandwidth is the range within which the BOR FDTD simulator is expected to compute accurate results.

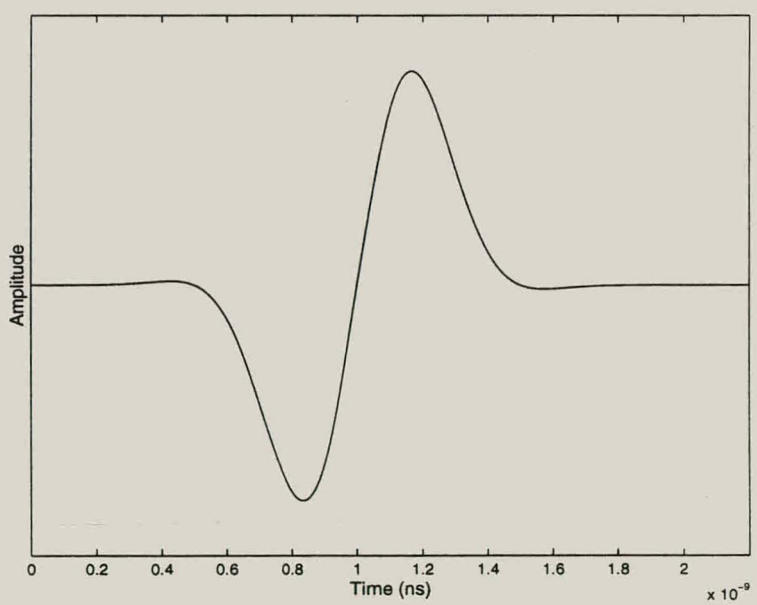

Figure 4.1: Incident Pulse Waveform in the Time Domain

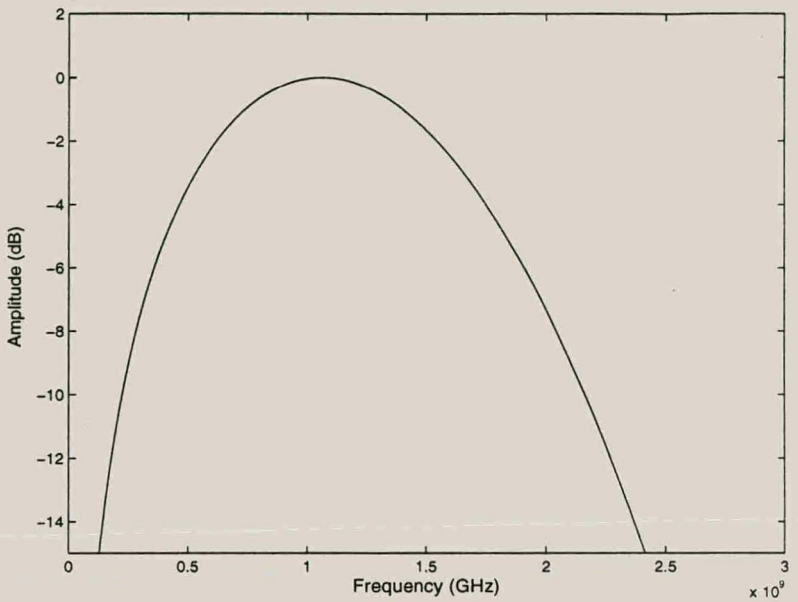

Figure 4.2: Incident Pulse Waveform in the Frequency Domain

4.3 Plane Wave Propagation, Reflection and Transmission

Given a linear homogeneous medium with intrinsic impedance $\eta = \sqrt{\frac{\epsilon}{\mu}}\ \Omega$, the wave velocity within this medium will be $v = \frac{1}{\sqrt{\epsilon\mu}}\ m/s$. Assume a layered medium with constitutive parameters as depicted in figure 4.3. The reflection coefficient is the ratio of the incident field to the reflected field at the interfaces between each adjacent layer and is given as $\rho = \frac{\eta_2 - \eta_1}{\eta_2 + \eta_1}$. The transmission coefficient is, similarly, the ratio between the incident field and the transmitted field at these interfaces and is given by $\tau = \frac{2\eta_2}{\eta_2 + \eta_1}$.

A BOR FDTD simulation was run with :

- $\zeta = 0.83$ [1]

[1] see equation (3.26) for the definition of ζ

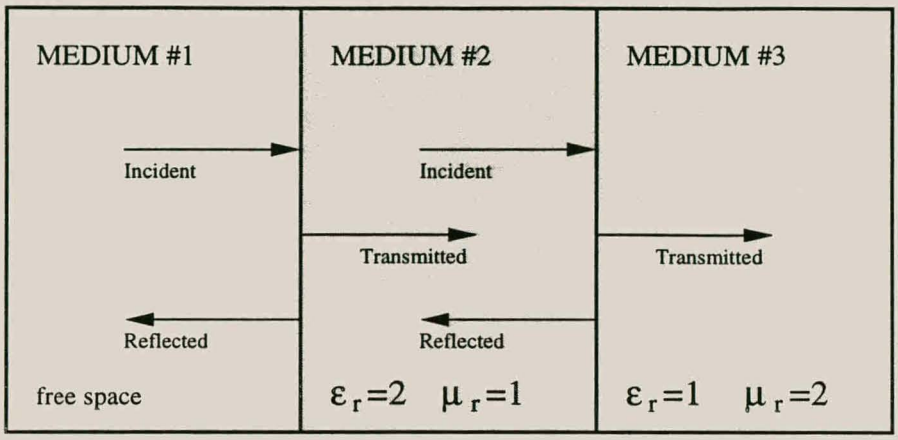

Figure 4.3: Plane Wave Incident on a Layered Medium

- 16 samples per free-space (centre frequency) wavelength
- 400 × 900 cell grid corresponding to a 0.7m radial dimension and a 1.6m depth dimension.
- the incident pulse described above with a spatial *waist* of $W = 0.2$m (see figure 3.5).

Table 4.3 shows the comparison between the theoretical wave velocities (in the direction of propagation) in the three respective media and those computed with the BOR FDTD simulator.

	Medium #1	**Medium #2**	**Medium #3**
ϵ_r	1.0	2.0	1.0
μ_r	1.0	1.0	2.0
Theoretical v(m/s)	299.8×10^6	211.99×10^6	211.99×10^6
BOR FDTD v(m/s)	299.61×10^6	211.85×10^6	211.85×10^6
% error	0.0634%	0.066%	0.066%

Table 4.1: Verification of Wave Speed for Layered Medium of Figure 4.3

The same simulated data as used above is used in the analysis of the reflection and transmission coefficients. The Gaussian spatial weighting given to the incident field will radiate from the source with a fixed angular or transverse dependence [16]. To accurately model normal plane wave incidence on the layered medium, the waist of the incident field needs to be made large so that the on-axis region remains relatively planar. This, however, will mean that the grid size will have to increase somewhat and consequently the required resources. For a reasonable sized grid, some *spreading* of the beam will occur and it will affect the reflection and transmission coefficient readings. For this reason a qualitative analysis is not given but plots are provided below at three different time steps to show that the wave behaves correctly at each interface between media. The arrows in these figures depict the direction of travel of the pulse-let. Figure 4.4 shows the incident pulse in free-space (medium #1). Figure 4.5 shows both the transmitted and reflected pulses from the first interface. The reflected pulse is inverted as expected. Figure 4.6 shows the reflected and transmitted pulse off the second (last) interface. Here the reflected pulse is not inverted as expected.

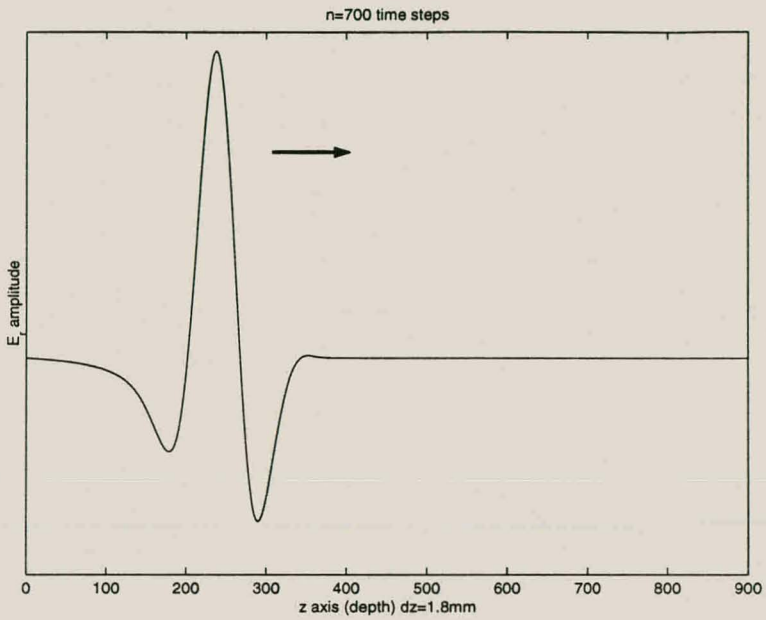

Figure 4.4: Incident Pulse in Free-Space.

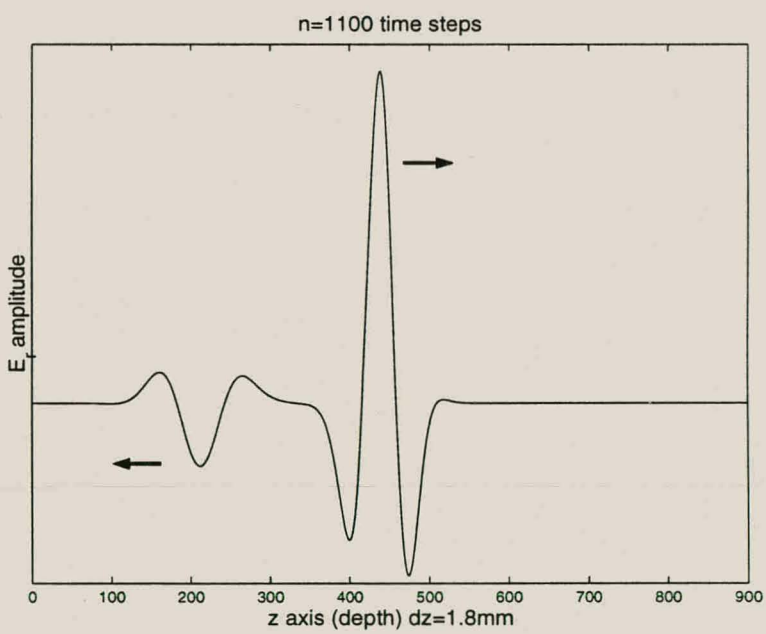

Figure 4.5: Reflection from First Interface.

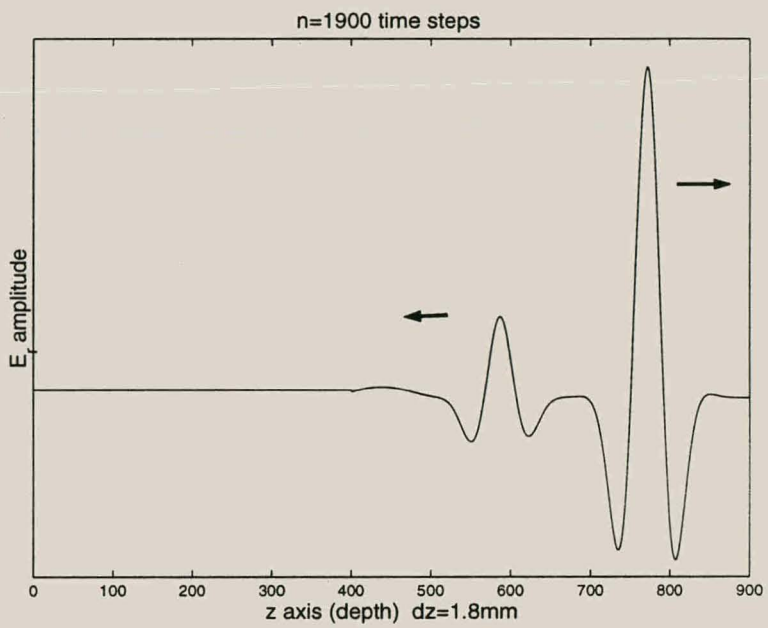

Figure 4.6: Reflection from Second Interface.

4.4 Scattering by Spheres

The plane wave scattering by a sphere is one of the classic scattering problems in electromagnetics and acoustics. The monostatic Radar Cross Section (RCS) of a conducting and a dielectric sphere is determined analytically and compared with the numerical results obtained with the BOR FDTD simulator. This analytical solution has been examined by many authors [18], however, most texts provide only the far field limit for the monostatic RCS cross-section. Of more academic interest to GPR simulations is the near field RCS where the scatterer is near or under the Rayleigh far field criterium.

The analytical solution derived here is adapted from Harrington [19] and Balanis [18] with emphasis placed on obtaining electric near field information. The formulation makes use of the widely used method of *separation of variables* for finding solutions to the spherical Helmholtz equation :

$$\frac{1}{r^2}\frac{\partial}{\partial r}\left(r^2\frac{\partial \psi}{\partial r}\right) + \frac{1}{r^2\sin\theta}\frac{\partial}{\partial \theta}\left(\sin\theta\frac{\partial \psi}{\partial \theta}\right) + \frac{1}{r^2\sin^2\theta}\frac{\partial^2 \psi}{\partial \phi^2} + k^2\psi = 0$$

A detailed discussion is provided in appendix E where it is shown there that common solutions include Associated Legendre functions (P_n^m), Spherical Bessel function ($z_n(kr)$) and Harmonic functions ($e^{-jm\phi}$). Computation of the final analytical solution requires extensive knowledge of these Bessel and Legendre functions and their recursive identities. [2] Refer to Bowman [20] and Watson [21] for detailed discussions on Bessel and Legendre functions.

For convenience, the fields are expressed as the superposition of vector field potential components transverse magnetic (TM) and transverse electric (TE) to r, that is, in terms of A_r and F_r. From appendix E.2, the electric and magnetic field solutions to the spherical Helmholtz equation become

[2] Appendix E contains the necessary discussions.

$$E_r = \frac{1}{j\omega\epsilon}\left(\frac{\partial^2}{\partial r^2} + k^2\right) A_r \tag{4.2}$$

$$E_\theta = \frac{-1}{r\sin\theta}\frac{\partial F_r}{\partial \phi} + \frac{1}{j\omega\epsilon r}\frac{\partial^2 A_r}{\partial r \partial \theta} \tag{4.3}$$

$$E_\phi = \frac{1}{r}\frac{\partial F_r}{\partial \phi} + \frac{1}{j\omega\epsilon r\sin\theta}\frac{\partial^2 A_r}{\partial r \partial \phi} \tag{4.4}$$

$$H_r = \frac{1}{j\omega\mu}\left(\frac{\partial^2}{\partial r^2} + k^2\right) F_r \tag{4.5}$$

$$H_\theta = \frac{1}{r\sin\theta}\frac{\partial A_r}{\partial \phi} + \frac{1}{j\omega\mu r}\frac{\partial^2 F_r}{\partial r \partial \theta} \tag{4.6}$$

$$H_\phi = -\frac{1}{r}\frac{\partial A_r}{\partial \theta} + \frac{1}{j\omega\mu r\sin\theta}\frac{\partial^2 F_r}{\partial r \partial \phi} \tag{4.7}$$

4.4.1 Incident and Scattered Fields

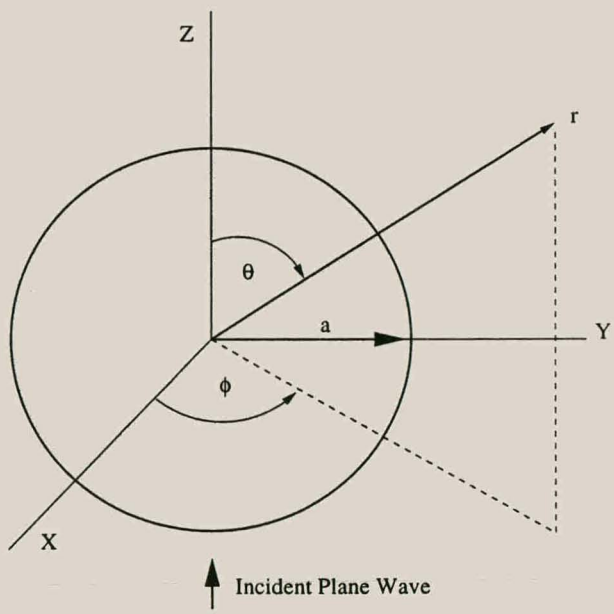

Figure 4.7: Plane Wave Incident on a Sphere

Assuming the incident electric field of a uniform plane wave is linearly polarised in the x

direction and is travelling along the z axis as depicted in figure 4.7. The electric field can be expressed as

$$\mathbf{E}^i = \hat{x}E_x^i = \hat{x}E_0 e^{-jkz} = \hat{x}E_0 e^{-jkr\cos\theta} \tag{4.8}$$

and transformed into spherical coordinates as

$$\mathbf{E}^i = \hat{r}E_r^i + \hat{\theta}E_\theta^i + \hat{\phi}E_\phi^i \tag{4.9}$$

where

$$\begin{aligned} E_r^i &= E_x^i \sin\theta\cos\phi \\ &= E_0 \sin\theta\cos\phi e^{-jkr\cos\theta} && (4.10) \\ E_\theta^i &= E_x^i \cos\theta\cos\phi \\ &= E_0 \cos\theta\cos\phi e^{-jkr\cos\theta} && (4.11) \\ E_\phi^i &= -E_x^i \cos\phi \\ &= -E_0 \cos\phi e^{-jkr\cos\theta} && (4.12) \end{aligned}$$

Following the procedures in appendices F.1 and F.2, the scattered fields can be expressed as

$$E_r^s = -jE_0\cos\phi\sum_{n=1}^{\infty} b_n\left[\hat{H}_n''^{(2)}(kr) + \hat{H}_n^{(2)}(kr)\right]P_n^1(\cos\theta) \tag{4.13}$$

$$E_\theta^s = \frac{E_0}{kr}\cos\phi\sum_{n=1}^{\infty}\left[jb_n\hat{H}_n'^{(2)}(kr)\sin\theta P_n'^1(\cos\theta) - c_n\hat{H}_n^{(2)}(kr)\frac{P_n^1(\cos\theta)}{\sin\theta}\right] \tag{4.14}$$

$$E_\phi^s = \frac{E_0}{kr}\sin\phi\sum_{n=1}^{\infty}\left[jb_n\hat{H}_n'^{(2)}(kr)\frac{P_n^1(\cos\theta)}{\sin\theta} - c_n\hat{H}_n^{(2)}(kr)P_n'^1(\cos\theta)\right] \tag{4.15}$$

where

$$\hat{H}_n^{\prime(2)}(x) = \frac{\partial \hat{H}_n^{(2)}(x)}{\partial x} \qquad \hat{H}_n^{\prime\prime(2)}(x) = \frac{\partial^2 \hat{H}_n^{(2)}(x)}{\partial x^2} \qquad P_n^{\prime 1}(u) = \frac{\partial P_n^1(u)}{\partial u}$$

and can be determined from the recursion identities (F.21-F.22).

4.4.2 Scattering from a Conducting Sphere

The boundary condition that needs to be met, on the circumference of a conducting sphere, is that the tangential **E** fields need to be zero.

$$E_\theta = E_\phi = 0 \quad \text{at} \quad r = a \tag{4.16}$$

These boundary conditions require that

$$\begin{aligned} b_n &= -a_n \frac{\hat{J}_n'(ka)}{\hat{H}_n^{\prime(2)}(ka)} \\ c_n &= -a_n \frac{\hat{J}_n(ka)}{\hat{H}_n^{(2)}(ka)} \end{aligned} \tag{4.17}$$

where $\hat{J}_n'(x) = \frac{\partial \hat{J}_n(x)}{\partial x}$. Equations (4.13-4.15) can be used in conjunction with b_n and c_n to obtain the final scattered field solution.

4.4.3 Scattering from a Dielectric Sphere

Assuming the region inside the sphere is of a known dielectric (ϵ_d, μ_d) and that the sphere lies in free-space (ϵ_0, μ_0). There will be, in addition to the field external to the sphere expressed by the potential equations (F.17), a field internal to the sphere. The boundary

conditions to be met at the surface of the sphere ($r = a$) are

$$E_\theta^+ = E_\theta^- \qquad H_\theta^+ = H_\theta^-$$
$$E_\phi^+ = E_\phi^- \qquad H_\phi^+ = H_\phi^-$$

in other words, the tangential **E** and **H** fields must be continuous. Equations (4.2-4.7) are used to determine the field components. Outside the sphere ($r > a$) equations (F.17) apply. After applying the boundary conditions, the b_n and c_n coefficients can be expressed as

$$b_n = \frac{-\sqrt{\epsilon_d\mu_0}\hat{J}_n'(k_0a)\hat{J}_n(k_da) + \sqrt{\epsilon_0\mu_d}\hat{J}_n(k_0a)\hat{J}_n'(k_da)}{\sqrt{\epsilon_d\mu_0}\hat{H}_n'^{(2)}(k_0a)\hat{J}_n(k_da) - \sqrt{\epsilon_0\mu_d}\hat{H}_n^{(2)}(k_0a)\hat{J}_n'(k_da)}a_n \tag{4.18}$$

$$c_n = \frac{-\sqrt{\epsilon_d\mu_0}\hat{J}_n(k_0a)\hat{J}_n'(k_da) + \sqrt{\epsilon_0\mu_d}\hat{J}_n'(k_0a)\hat{J}_n(k_da)}{\sqrt{\epsilon_d\mu_0}\hat{H}_n^{(2)}(k_0a)\hat{J}_n'(k_da) - \sqrt{\epsilon_0\mu_d}\hat{H}_n'^{(2)}(k_0a)\hat{J}_n(k_da)}a_n \tag{4.19}$$

Only the exterior fields are of interest in computing the far field RCS, therefore the vector potential fields inside the sphere have not been included in deriving the above. Equations (4.13-4.15) are used in conjunction with b_n and c_n above to obtain the final solutions to the external scattered field components.

4.4.4 Monostatic Radar Cross Section

The monostatic RCS is defined as

$$\sigma_{3D}(\text{monostatic}) = \lim_{r\to\infty}\left(4\pi r^2\frac{|\mathbf{E}^s|^2}{|\mathbf{E}^i|^2}\right) \tag{4.20}$$

For a linearly x-polarised incident plane wave travelling along the z-axis, the field expressions must firstly be reduced for observations towards $\theta = \pi$. The copolar component of the scattered field, E_x^s, then becomes the field of interest. From figure 4.7 and the coordinate

conversion equation (A.1), this copolar component can be obtained by evaluating

$$E_x^s = E_\theta^s \cos\theta \cos\phi|_{\substack{\theta=\pi \\ \phi=\pi}} \tag{4.21}$$

The time harmonic incident field is obtained from equation (4.11)

$$E_\theta^i|_{\substack{\theta=\pi \\ \phi=\pi}} = E_0 \exp(-jkr) \tag{4.22}$$

The theoretical RCS can be determined from equations (4.11) and (4.14) for both conducting and dielectric spheres by noting the correct values of b_n and c_n. The far field case makes use of the asymptotic formula, $\hat{H}_n^{(2)}(kr) \rightarrow_{kr\rightarrow\infty} j^{n+1}e^{-jkr}$ and retains only the $1/r$ varying terms to produce the well known identity below (for conducting spheres) and is depicted in figure 4.8.

$$\sigma_{3D}(\text{monostatic}) = \frac{\lambda^2}{4\pi}\left|\sum_{n=1}^{\infty}\frac{(-1)^n(2n+1)}{\hat{H}_n'^{(2)}(kr)\hat{H}_n^{(2)}(kr)}\right|^2$$

As mentioned, however, the far field approximation is not of direct interest here other than as a reference for correctness. Equation (4.14) as stated is thus used in the RCS computation. Their are, however, singularities in this equation at $\theta = 0$ and $\theta = \pi$. The values at these singularities, however, can be evaluated explicitly using the relations

$$\begin{aligned} -\left.\frac{P_n^1(\cos\theta)}{\sin\theta}\right|_{\theta=\pi} &= (-1)^n\frac{n(n+1)}{2} \\ \sin\theta P_n'^1(\cos\theta)|_{\theta=\pi} &= -(-1)^n\frac{n(n+1)}{2} \end{aligned}$$

The BOR FDTD simulator relies on a cylindrical coordinate system. The x directed electric field in this case is the E_ρ field at $\phi = 0$ (see figure 2.1).

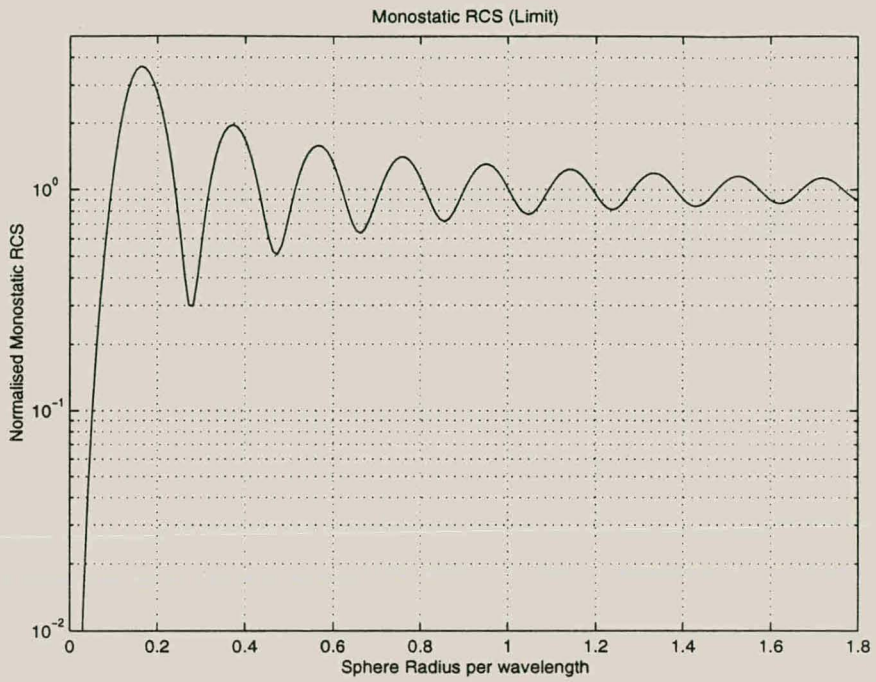

Figure 4.8: Monostatic Radar Cross Section (far field case)

4.4.5 Results

A few cases are considered where an isolated conducting or dielectric sphere lies in free-space some distance from the observation point. A small DC component appears in the BOR FDTD result which is not shown in the results. This is an expected phenomena and is a function of grid capacitance introduced by the non-physical source model [22]. This component will always appear unless charge dynamics are taken into account during the FDTD formulation. Fortunately, GPR systems do not rely on such low frequency information and this component can effectively be filtered out during post-processing.

The results in this section are all computed using the incident pulse described in section 4.2. The spatial step (Δ) is taken at 30 samples per free-space wavelength (for numerical dispersion suppression and other stability reasons described in section 3.8), except for the dielectric sphere where the shortest wavelength in the problem space is used. Furthermore,

the temporal step is taken just below the Courant limit as $\zeta = 0.83$.

The RCS from a conducting sphere of radius $50cm$ at a distance of $3m$ from the observation point is shown in figure 4.9. The RCS from a dielectric sphere ($\epsilon_r = 1.2$) of the same size and distance is shown in figure 4.10. The far field theoretical solution in figure 4.8 is depicted in terms of spherical radii per wavelength and it is helpful to see a similarly represented numerical result is depicted in figure 4.11. [3]

The results depicted in this section are normalised to the radius of the spherical scatterer, no other processing is performed on the data to make the numerical and theoretical results fit. With this in mind, the comparison between the known solution and the BOR FDTD simulated results is very favourable.

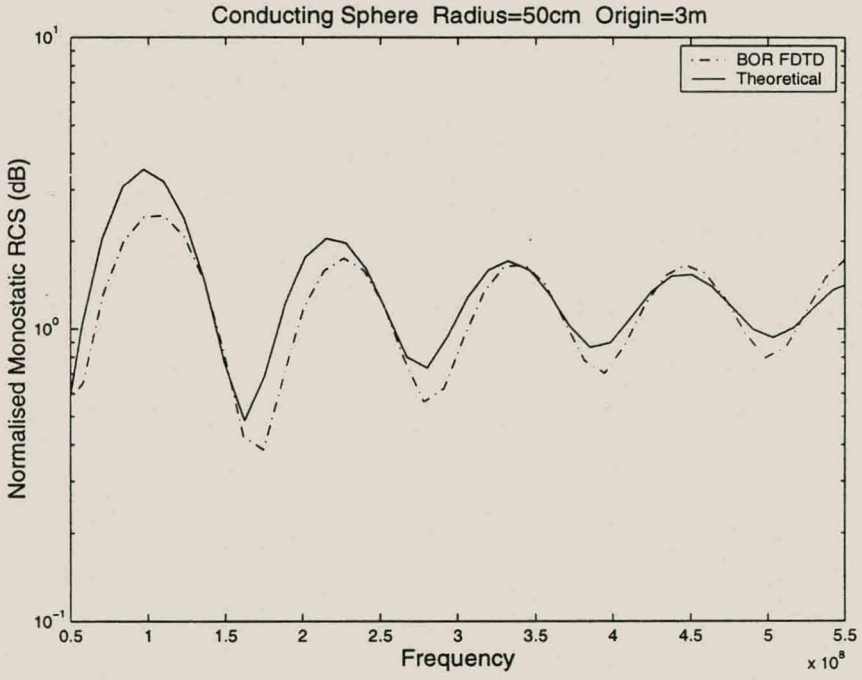

Figure 4.9: RCS of Conducting Sphere of Radius=$50cm$

[3] The analytical solution is often referred to as the *Mie solution* in optics

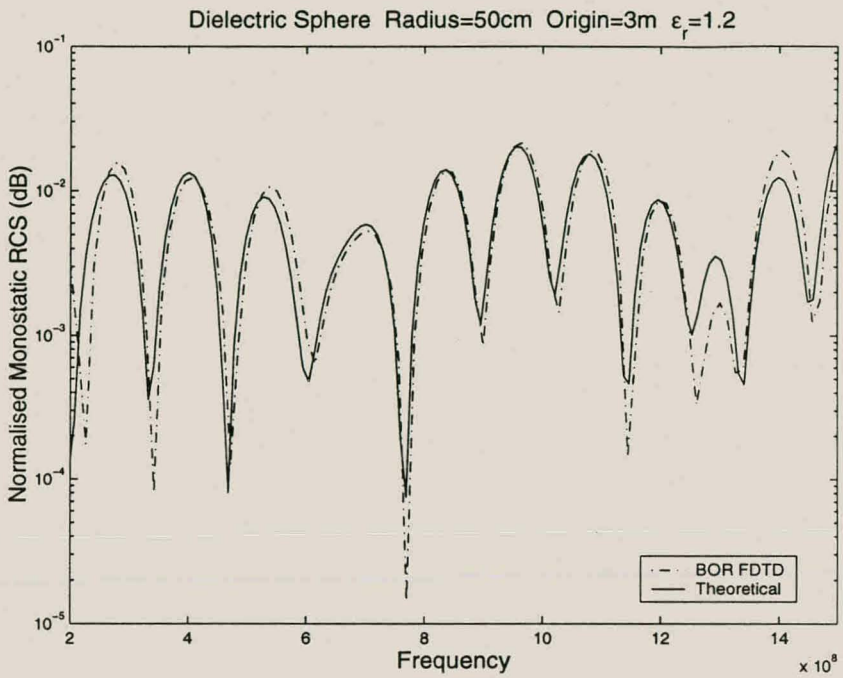

Figure 4.10: RCS of Dielectric Sphere ($\epsilon_r = 1.2$ of Radius=$50cm$)

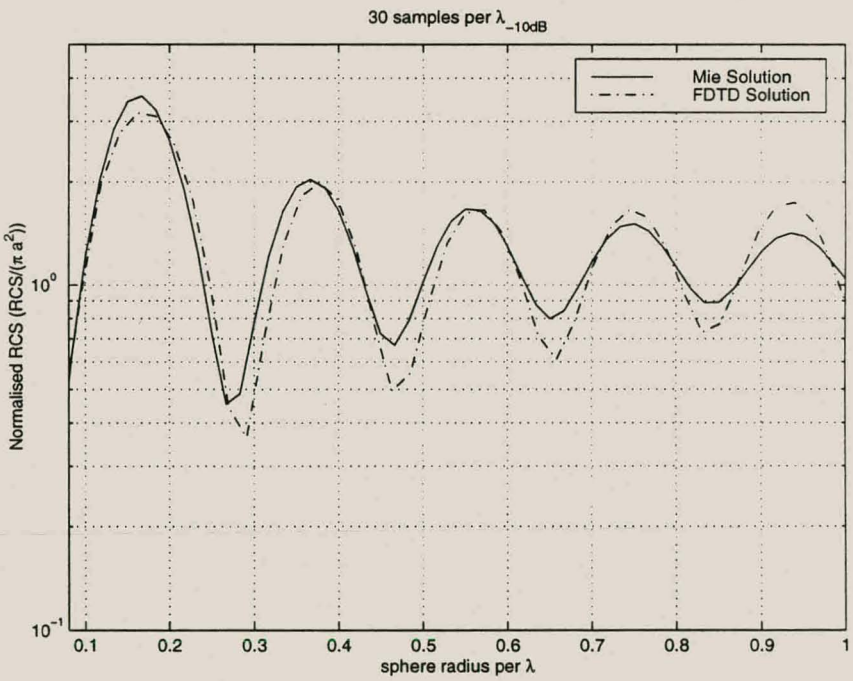

Figure 4.11: RCS of Conducting Sphere vs Radius in Wavelengths

4.5 Conclusion

With a reasonable spatial step size of 30 samples per wavelength and running at just below the Courant limit, the BOR FDTD simulator behaves favourably under the conditions tested. The wave velocity is correct to within a fraction of a percent, and the wave interacts with layered media and spherical scatterers as predicted by theory. The formulation is thus complete and the BOR FDTD simulator can be confidently applied to complex scattering configurations.

Chapter 5

Data Model Generation

5.1 Rotational Symmetry Requirement

The rotational symmetry requirement introduces some limiting conditions in terms of the range of geometrical shapes that can be modelled in a BOR FDTD grid. Fortunately, a large enough percentage of land-mines can be considered to be rotationally symmetric [5] to warrant treating them on their own. Stratified ground layers can be implemented with relative ease. Rough surface air-ground interfaces can also be implemented, however, the rough conditions would be seen as ripples after 360° rotation around the z axis. The implementation of such an interface, although not fully 3-D spatially variant, will still introduce some measure of real world surface scattering effects. Unfortunately though, off-centre objects cannot be modelled. Possible coupling effects of surrounding clutter with the land-mine (or other targets) is therefore not included in the model, which simply superimposes the target and clutter returns.

5.2 Design Philosophy

The motivation is to generate large amounts of GPR simulations that model real world conditions as accurately as possible, within a reasonable time frame. The emphasis in this thesis, however, is not being placed on how well real world conditions can be modelled within the BOR FDTD framework but rather on a *feasibility of detection* principle. In other words, of more immediate concern is a rough estimate of how separable, in a pattern recognition sense, the simulated GPR returns from buried targets are from their surroundings and from targets. This information is extremely valuable in the initial design stage of a GPR project, since the designer is able to ascertain, from the readily available simulated data, whether to move on to a more expensive and time consuming practically oriented stage or not. This information serves as a platform for testing detection techniques, in principle, quickly and cheaply.

Soil attenuation and levels of contrast between the dielectric parameters of the target and its surrounding soil are two major factors that affect the returned GPR echo. These conditions have to be implementable in the model. Accurate GPR data generation requires knowledge of the constitutive properties of the soil, land-mines and any non-mine scatterers inserted into the problem space. This can become quite a complex process, therefore certain assumptions are made to simplify the model generation, e.g.

- Stratified, sub-surface, soil layers are assumed linear and homogeneous.
- Simplified target scatterer geometries and constitutive parameters are used.
- Only a finite set of soil conditions are modelled.
- Only a finite set of different target scatterer types are considered.

These assumptions will also have various effects from a pattern recognition viewpoint.

5.3 Soil Layers

Some in-depth work has gone into accurate classification of soil types in terms of relative permittivity and attenuation [23, 24]. Experimental studies show that the relative permittivity of soil increases with an increase in moisture content and decreases with an increase in frequency, while conductivity rises with both frequency and water content [24]. There are a variety of different soil types to consider so the field is narrowed to consider only

- dry, sandy soil ($\epsilon_r = 2.5 - 6$, $\sigma = 100^{-6} - 10^{-3}$S/m) and
- slightly moist [1] soil ($\epsilon_r = 10 - 20$, $\sigma = 10^{-3} - 0.1$S/m).

In Western Europe of course, very moist soil would also be significant. Subsurface soil layers are modelled as stratified. This is assumed from the fact that pressure effects below the earth's surface should compact soil layers, making them approximately flat over typical GPR focus regions. The air-ground interface is however not affected in this way and, as suggested in section 5.1, are modelled as randomly rough surfaces.

5.4 Random Rough Surface Generation

To generate ensembles of random surfaces, the method of Thorsos [25] is used. A Gaussian roughness power spectral density $W(K)$ is generated with Gaussian statistics. A surface profile $f(x)$ is then obtained by inverse Fourier transforming the spectrum. The result is depicted in figure 5.1.

The surface realisation will be discretised according to the spatial step sizes, Δz and $\Delta \rho$, required for stability of the BOR FDTD simulator. These step sizes are assumed typically

[1] up to 20% moisture content

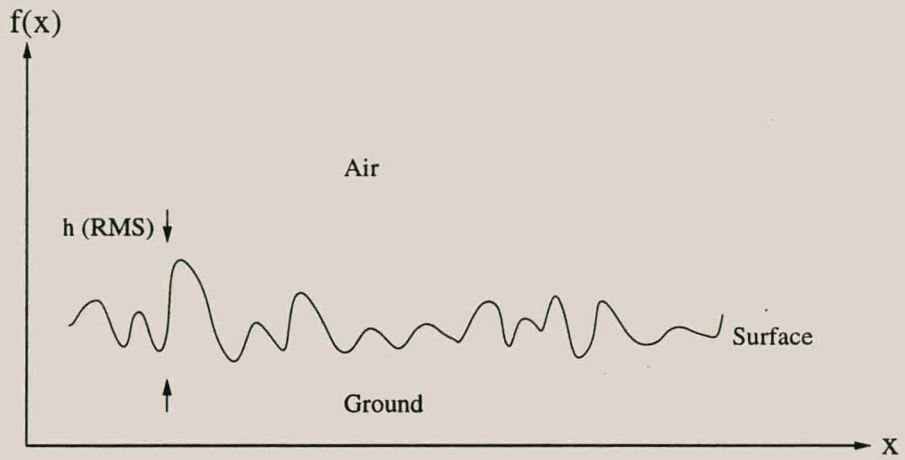

Figure 5.1: Example of Rough Surface Realisation.

small enough to allow for correct approximation of the surface without introducing spatial aliasing. [2]

5.4.1 Method

The rough surface is generated by passing a white Gaussian noise process through a filter that has the same frequency characteristic as the desired power spectrum of the rough surface [26].

According to the FDTD method, each surface consists of N discrete points spaced Δx meters apart over a total length of $L = N\Delta x$ meters. The Gaussian surface spectral density, $W(K)$, is zero mean with a root mean square (RMS) height of h^2 and a correlation length of l. K denotes the surface spatial wavenumber.

$$W(K) = \frac{lh^2}{2\sqrt{\pi}} \exp\left[-\frac{K^2 l^2}{4}\right] \tag{5.1}$$

[2] This is a fair assumption since the steps sizes are usually in the order of a few millimetres.

$W(K)$ is normalised with respect to h^2

$$\int_{-\infty}^{\infty} W(K)dK = h^2 \tag{5.2}$$

$W(K)$ is related to $f(x)$ with the aid of ensemble averaging (<>)

$$W(K) = \lim_{L\to\infty} \frac{1}{2\pi} \left\langle \frac{1}{L} \left| \int_{-L/2}^{L/2} f(x)e^{-iKx}dx \right|^2 \right\rangle \tag{5.3}$$

The desired surface realisations are determined using the inverse Fast Fourier Transform (FFT)

$$f(x_n) = \frac{1}{L} \sum_{j=-N/2}^{N/2-1} F(K_j)x_n \tag{5.4}$$

where, for $l \geq 0$

$$F(K_j) = \sqrt{2\pi L W(K_j)} \begin{cases} \frac{[N(0,1)+iN(0,1)]}{\sqrt{2}} & j \neq 0, N/2, \\ N(0,1) & j = 0, N/2 \end{cases} \tag{5.5}$$

The wavenumber is determined as $K_j = 2\pi j/L$. Conjugate symmetry is used for $j < 0$ ie. $F(K_j) = F(K_{-j})$. Each time $N(0,1)$ appears it denotes an individual random sample taken from a zero mean unit variance Gaussian distribution.

The nature of the discrete spectrum causes correlation at the ends of each surface [27]. In practice, therefore, longer surface realisations of N' points are generated and the required N points are cut from it to reduce correlation. N' is taken here to be at least three times N, furthermore, N is *cut out* from the middle of N'.

A polar form of the Box-Muller transform [28] is used to transform samples generated using an uniform pseudo-random number generator into a normal distribution. The MATLAB code that performs the above rough surface generation operations can be found in the

appendix G.

5.4.2 Results

The surface realisations to be modelled are chosen with RMS height values ranging over $h = 50$mm to 1mm and correlation lengths between $l = 0.25$ and 0.05. The four surface extremes are depicted in figure 5.2 and are comparable to those published in [29]. It is important to note that increasing the correlation length results in a *smoother* surface.

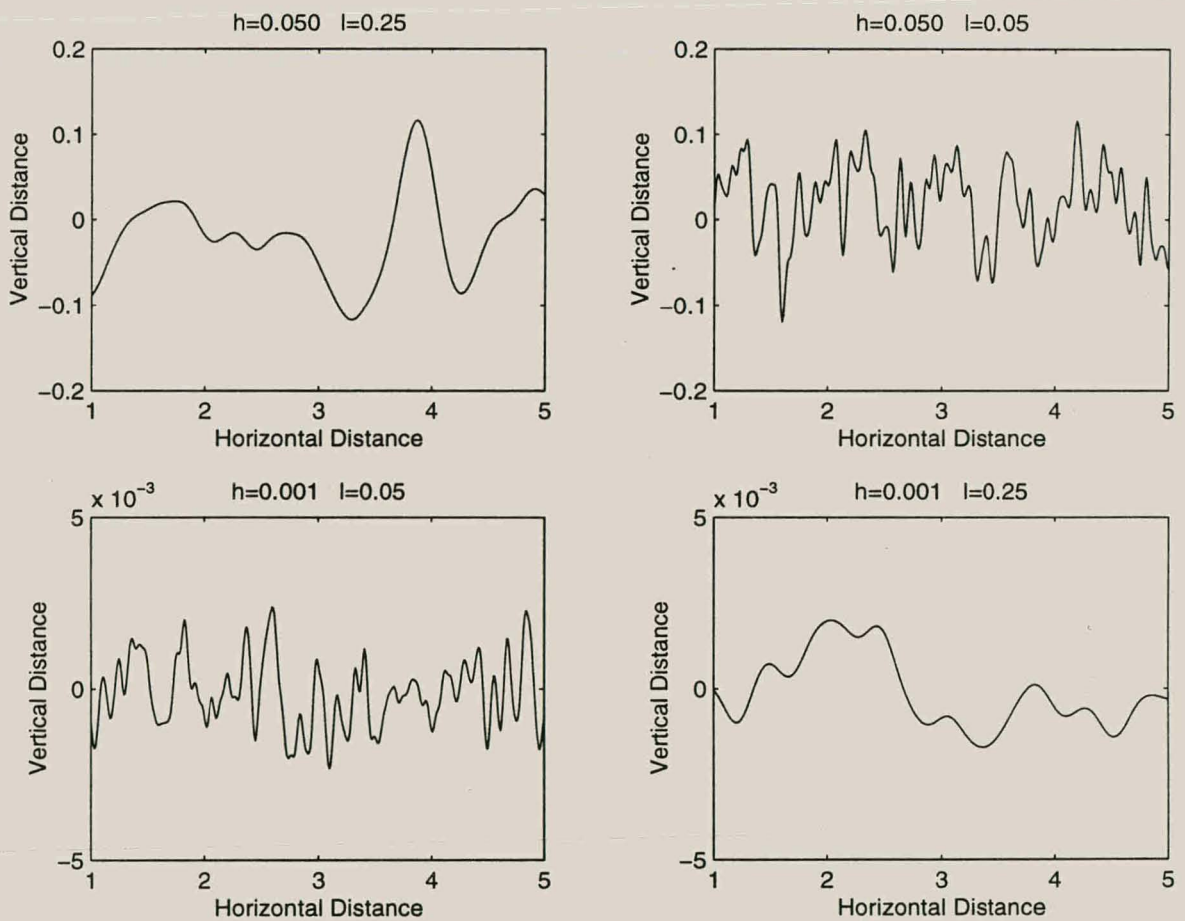

Figure 5.2: The Four Extreme Rough Surface Realisations (all distances in meters).

5.5 Target Model Classes

Six classes of targets were chosen denoting the presence of land-mines or clutter. A seventh class which denotes the absence of any targets is also included. This latter class comprises solely of an air-ground interface and zero, one or more stratified layers as described in sections 5.3 and 5.4.

Four of the six target classes are chosen to represent common land-mines of different composition, size and burial depth. The remaining two represent general clutter.

5.5.1 Land-Mine Classes

The major visible distinction between land-mines can be made in terms of size. Anti-Tank (AT) mines are generally much larger than the Anti-Personal (AP) mines. Shape also plays a major role, however, the rotational symmetry requirement dictates that only cylindrical or round mines can be considered.

Another important distinction is in their composition. Land-mines can range from having full metallic casings to having a minimal metallic content inside a plastic casing. Nearly all AP mines have enough metal content to be detected with metal detectors [1], however, mineralised soils and metallic clutter (eg. cans, nails, rubbish) require more advanced techniques to be employed. Typical explosive compositions include TNT, RDX and Comp B.

A last consideration should be the burial depth. Bounding fragmentation mines need to be buried quite shallow to be effective while larger AT and more sensitive AP mines can be buried a lot deeper. Generally though, land-mines are commonly found up to a burial depth of 50cm [23]. In the models described below, provision is made for mines that have been

covered with soil. Provision is not made for mines that have been uncovered since they can more readily be detected optically.

5.5.1.1 Metallic Land-mines

Two of the four land-mine classes are chosen as having metallic casings. These are easily modelled in the BOR FDTD simulator as PEC boundaries. The two mines chosen are the M20 and Valmara 59 depicted in figures 5.3 and 5.4 respectively. The M20 is a very large, heavy AT blast mine modelled to have a burial depth of between 3cm and 50cm. The geometric model used for the simulations is depicted in figure 5.5. The Valmara 59 is a bounding fragmentation AP mine commonly shallow buried up to 20cm. Its geometric model is depicted in figure 5.6. The Valmara 59 has protruding metal spikes which are not modelled because of the BOR requirement. These prongs are most likely to introduce effects at higher frequencies [30] and are ignored here for simplicity.

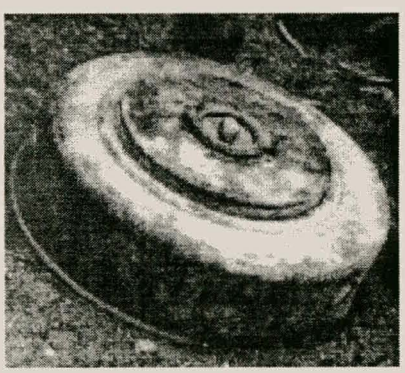

Figure 5.3: M20 AT Land-mine [31].

Figure 5.4: Valmara 59 AP Land-mine [31].

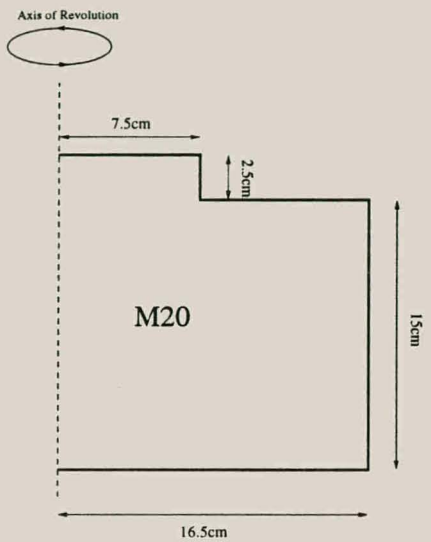

Figure 5.5: M20 Model [32].

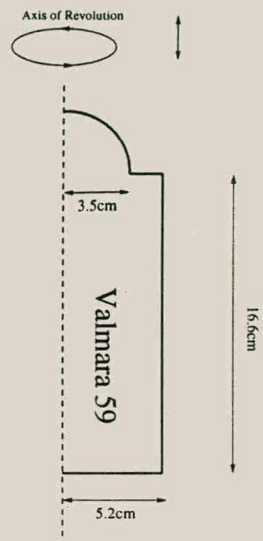

Figure 5.6: Valmara 59 Model [31].

5.5.1.2 Plastic Land-mines

The remaining two land-mines are chosen as having plastic cases of relative permittivity of $\epsilon_r = 2.67$ [23]. For simplicity, the metal striking pins inside the mines are omitted from the models. The two mines considered are the very small R2M2 and the common PMN2 depicted in figure 5.7 and 5.8 respectively. Both the PMN2 and the R2M2 are AP blast mines. They are modelled as containing TNT [3] which has relative permittivity $\epsilon_r = 2.9$ and conductivity $\sigma = 10^{-3}$S/m. The casing is considered quite thin compared to the total volume of these mines (a fraction of a wavelength) and is consequently ignored in the geometric models depicted in figures 5.9 and 5.10. Just like with the Valmara mine, the PMN2 has protruding dials which are ignored in this model.

[3] The R2M2 actually contains RDX explosive but in order to maintain generality it is treated as being similar to the PMN2.

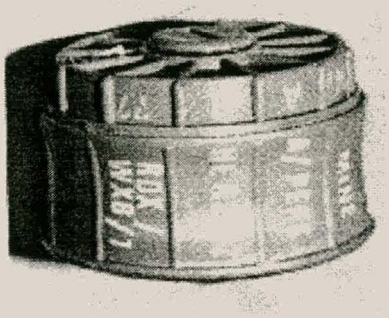

Figure 5.7: R2M2 AP Land-mine [31].

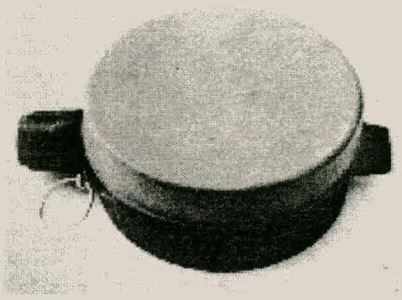

Figure 5.8: PMN2 AP Land-mine [31].

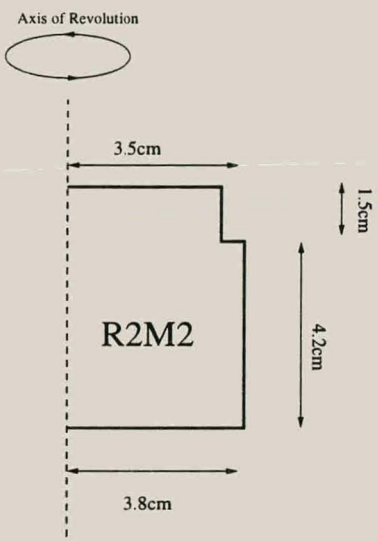

Figure 5.9: R2M2 Model [31].

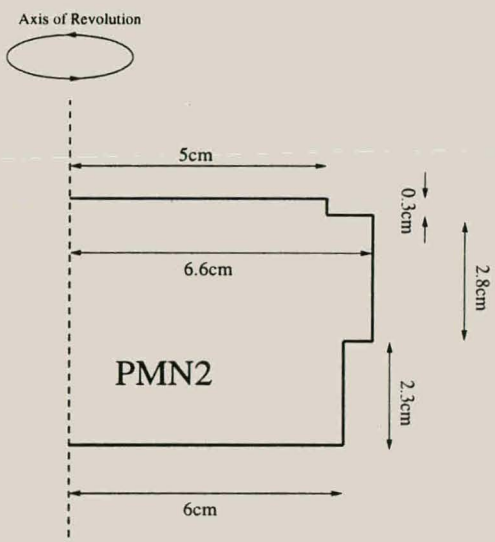

Figure 5.10: PMN2 Model [32].

5.5.2 Non-Mine Classes

The remaining two classes refer to non-mine scatterers. The first obvious choice are rocks and they are very simplistically modelled as spheres of radius varying from 1cm to 50cm and buried up to 50cm below the surface. In this way rocks can be generated to cover all the possible sizes of the other targets. They are further modelled with relative permittivities of $\epsilon_r = 5 - 7$ and conductivity $\sigma = 10^{-9} - 1^{-6}$S/m.

Lastly a metallic beverage can (figure 5.11) is chosen since its size and shape are similar to the Valmara 59 mine. They are also a common form of ground clutter and represent any

average sized metallic obstacle. The cans are modelled as PEC's and are inserted, in the model, up to 50cm. The geometric model is shown in figure 5.12.

Figure 5.11: Metallic Beverage Can.

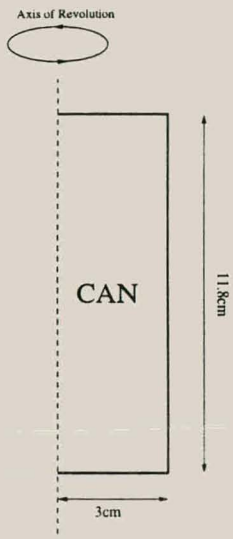

Figure 5.12: Metallic Beverage Can Model.

5.6 Antenna

A physical antenna model is not inserted in the model since it is felt that no pertinent information, that would enhance detection, would be *gained* from its inclusion. An antenna model would only further serve to increase the accuracy of the formulation in terms of the reception characteristics of the GPR and would be problem specific. The motivation for this decision is in accordance with the overall design philosophy and in maintaining generality of the model.

The transmitting antenna is therefore modelled using the Gaussian beam model approach discussed in section 3.9.1 and [16]. On-axis illumination (which is required for the $k = 1$ mode BOR formulation for the FDTD method) implies a monostatic antenna configuration, therefore, a receiving antenna need not be included in the model. The received time-domain scattered signal is simply recorded off the central axis where it is assumed to be a maximum,

as opposed to averaging the fields across a finite aperture width in space. The source plane and corresponding receiving point are modelled to approximate a GPR held 10cm above the earth's surface, in free-space.

Thermal receiver noise can be included in the problem as well. Such noise is relevant from a detection and signal processing point of view and will be discussed in the next chapter. It is considered to be additive noise and is therefore not necessary to include it within the FDTD simulation but rather in a post-processing phase.

5.7 Data Acquisition

A database of BOR FDTD simulated GPR returns is generated by concurrently shelling out randomly generated model configurations to numerous computers in parallel. Figure 5.13 shows a possible representation model of the BOR FDTD problem space.

The model generator starts by inserting a random rough air-ground interface, as described in section 5.4.2, 10cm below the source plane. A maximum of up to $N = 3$ three stratified soil layers can be inserted below this layer with equal probability. The first layer has a 15% probability of being modelled as wet sandy soil with $\epsilon_r = 10 - 20$ and $\sigma = 10^{-3} - 0.1\text{S/m}$. This possible wet layer is only modelled to be up to 4cm deep so as to represent typical dry, African soil conditions. The remaining lower layers are modelled as dry sandy soil with $\epsilon_r = 2.5 - 6$ and $\sigma = 100^{-6} - 10^{-3}\text{S/m}$.

Once the soil conditions have been set up, one of the seven possible targets classes are inserted with equal *a priori* probability.

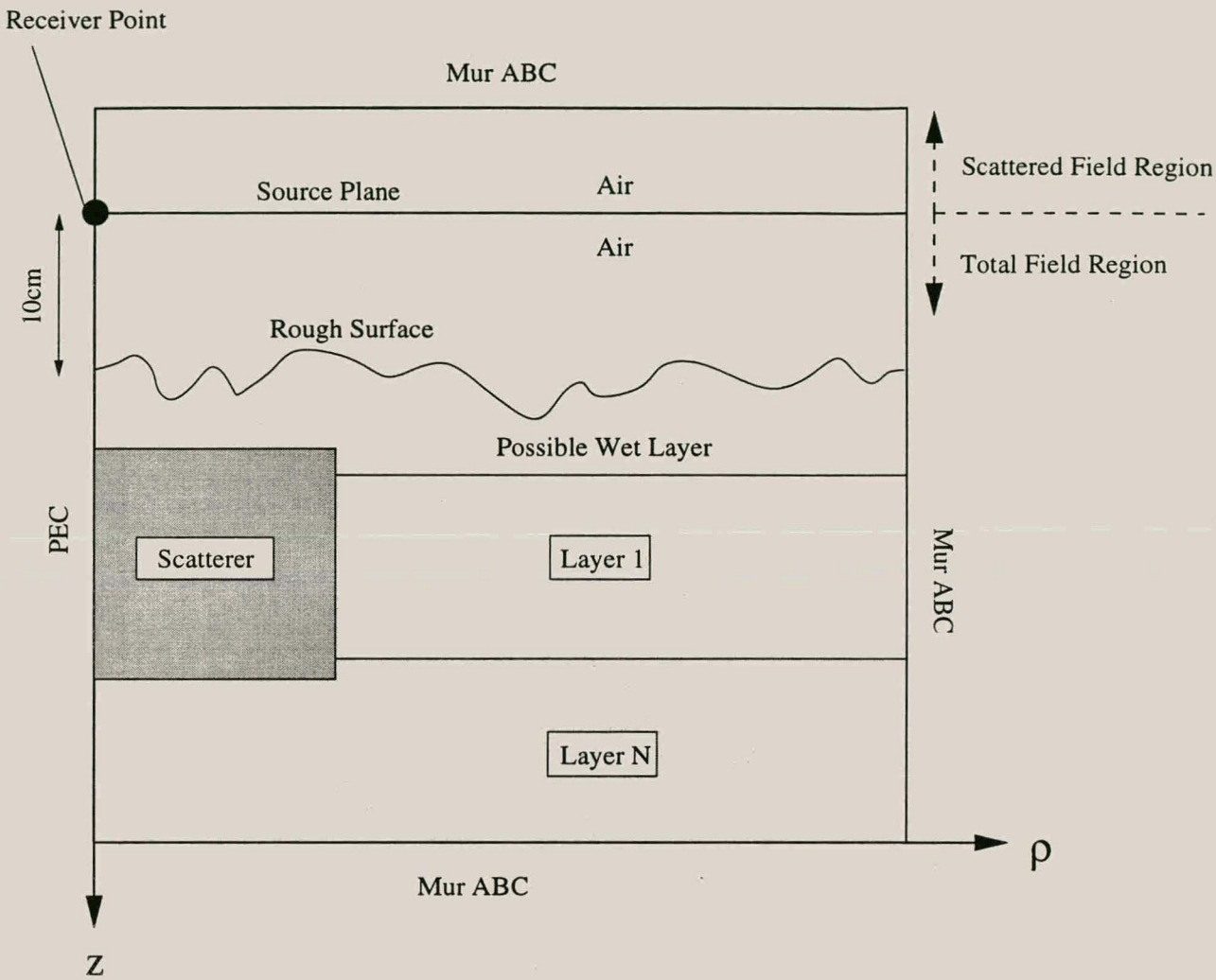

Figure 5.13: Problem Space Model.

5.8 Discussion

The simplified model, generated as described above, follows closely to the design philosophy prescribed in section 5.2. The seven classes of conditions considered are merely a small subset of possible real world conditions but are considered to be representative enough for a *proof of principle*. The clutter effects that are considered, in the model, are the interactions of the scattered fields from the targets and the surrounding stratified layers, the rough surface scattering and soil attenuation.

Typical grid sizes extend up to approximately $1.5m^2$ for the larger targets.

Chapter 6

Feature Extraction

6.1 Introduction

The BOR FDTD method described previously provides large amounts of simulated time-domain GPR data for post processing. This data contains all the information that would be contained from a GPR aimed directly above a land-mine buried in a lossy, stratified soil environment with a rough air-ground interface. The available data is generated for a number of model conditions and a number of targets. With a sufficient amount of this data, statistical pattern recognition techniques can be applied to some or other distinguishing features of the data for identification purposes.

The data obtained from a single *down cut* is often referred to as an A-scan [33] as seen in figure 6.1. A row of A-scans spaced a certain distance apart is called a B-scan and, when extending to three dimension, yields a C-scan. The C-scan is used for SAR inverse imaging and in conjunction with image processing techniques can be a powerful tool. The BOR requirement, unfortunately, does not allow the modelling of off-centre objects without considering the higher-order Fourier modes. The A-scans on their own do not exploit

the cross-range spatial properties of the scattered signals [32]. Each A-scan does, however, contain a full time history of the wave evolution through the problem space and the interactions between the scatterers and their surrounding media.

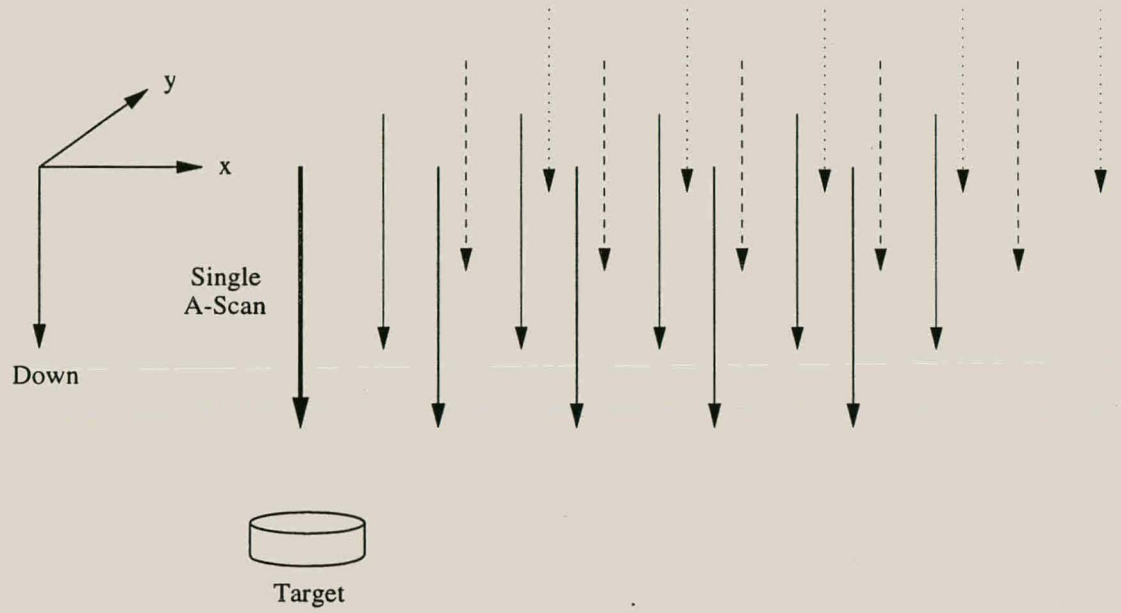

Figure 6.1: A-scan, B-scan and C-scan Configurations.

6.2 Qualitative Discussion

The GPR model used here is primarily a near field problem. In the near field the cross-polarised fields are assumed to be negligible and thus the copolar components become the fields of interest. With the incident pulse designed to be linearly polarised in the $\hat{x}$ direction (see Chapter 3.9.1) and travelling along the z axis, only the $\hat{x}$ component of the scattered fields at the origin need be used for post-processing. From figure A.1 and the coordinate conversion relations described in appendix A, on-axis excitation implies $\phi = 0$ and $\theta = \pi$, therefore, the radial electric scattered field component at the origin generated by the BOR FDTD simulator is used to represent this copolar scattered field component.

A target excited by a short time pulse, typically displays scattering characteristics in what can be described as *early-time* and *late-time* responses. The early-time response includes the initial diffraction of the incident field that occurs in and on the target body. The late-time response of the target includes resonances that occur as result of multiple diffractions, or creeping-waves, around the targets (these are especially prominent with conducting targets) and reverberations of the fields within penetrable targets. Further reverberations will also exist as a result of fields that *bounce* between the stratified soil layers. The scattered fields from the target scatterers themselves can interact significantly with surrounding soil layers too.

The strength of these natural resonances depends largely on the contrasts between different scattering bodies. This is expected from simple reflection coefficient theory where, the larger the differences between the equivalent medium impedances, the larger the reflected pulses are expected to be. Clearly, when the dielectric properties of plastic mines closely resemble those of the soil properties, as they are generally designed to be, the reflected signals and resonances are not expected to be particularly large. For this reason, land-mine detectors often wet the ground, where possible, to increase the relative permittivity of the soil and thus possibly increase the strength of reflections from such contrasts. Conducting targets reflect the entire incident pulse and the late-time resonances associated solely with such targets are primarily a result of creeping-waves. Metallic mines have consequently been shown to be associated with typically low-Q resonances [32].

Target size and depth will play a significant role too in the resonances obtained by observation of the A-scans. If there are strong reverberations between the targets and surrounding soil layers and ground surfaces, these resonances will become prominent in the signal. Target depth and size, however, will be more easily determined using 3-D spatial inverse imaging techniques and will be extremely difficult using only single A-scans. Size and depth is, however, important information since it will give insight into how information in the signal pertains to local interactions between the target and surrounding clutter.

The radial electric scattered field from a problem space involving a rough air-ground interface and a buried metallic beverage can is shown in figure 6.2. The first reflection from the air-ground interface is usually the biggest one and is clearly marked in the figure. The scattering from the can is only visible from about 7ns onwards. This first reflection contains a significant portion of the total energy received and can be gated out in time providing only there is the assurance that the target class does not lie within this region, ie. close to the surface. This is not the case with the model presented in Chapter 5 and therefore the detection procedure has to take these features into account.

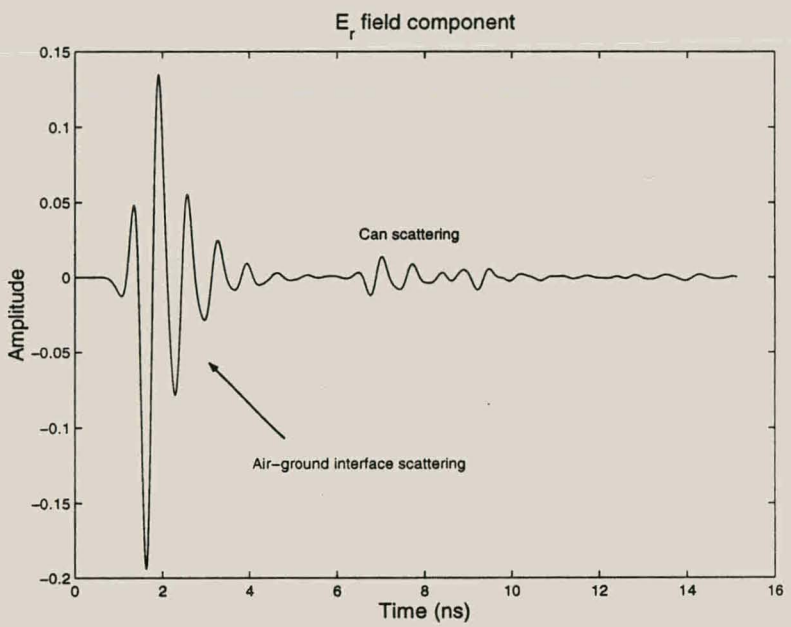

Figure 6.2: A-scan for a Can.

Figures 6.3 and 6.4 show typical radial electric scattered field returns from a buried PMN2 and M20 mine respectively. These two plots aid in depicting the effects of burial depth and target size. In figure 6.3 two reasonably undistorted reflections from ground layers are evident just before 5ns and just after 20ns. The section between these pulses contains the scattered field response of the plastic mine. In contrast with figure 6.4, the M20 mine (being much larger than the PMN2 mine and metallic) results in a larger overall scattered

signal. It is more difficult, however, to distinguish between the possible reflections from buried soil layers and the actual target resonance. If one of the targets was buried at the same level as a stratified soil layer, the relative size of the target would play an important role in the amount of energy of the returned signal, at that depth, being attributed to the target scattering alone. In figure 6.5, the ground surface reflection at 1ns is very discernible. At 4ns though, the first stratified soil layer *masks*, to a certain extent, the scattering time information from a can buried at roughly the same depth.

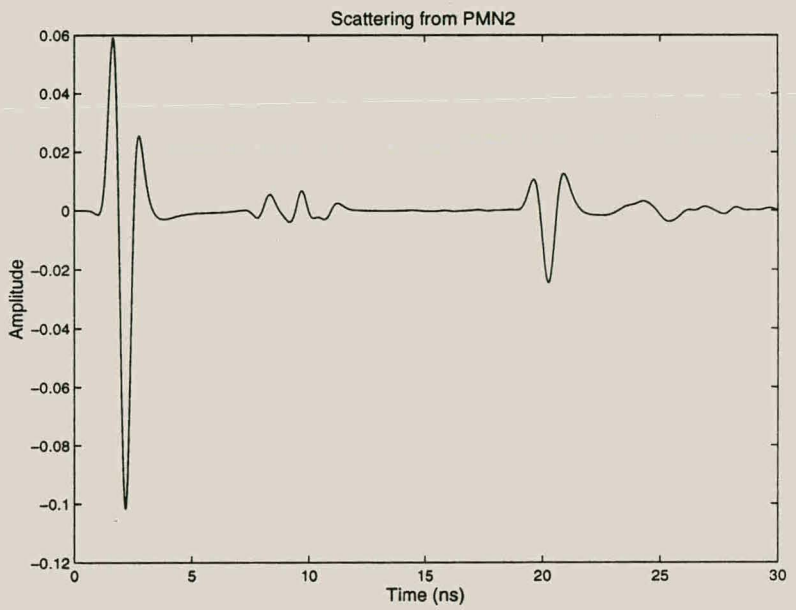

Figure 6.3: A-scan for a PMN2 Mine.

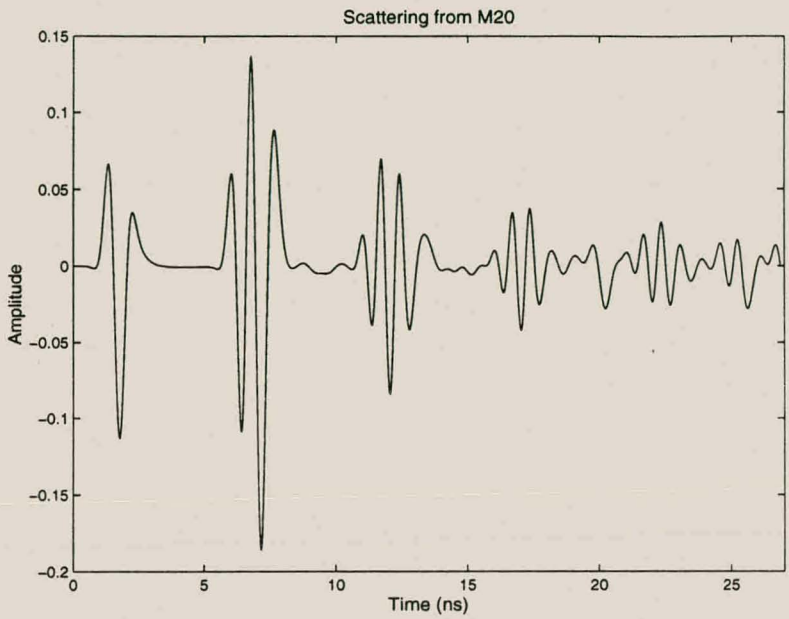

Figure 6.4: A-scan for a M20 Mine.

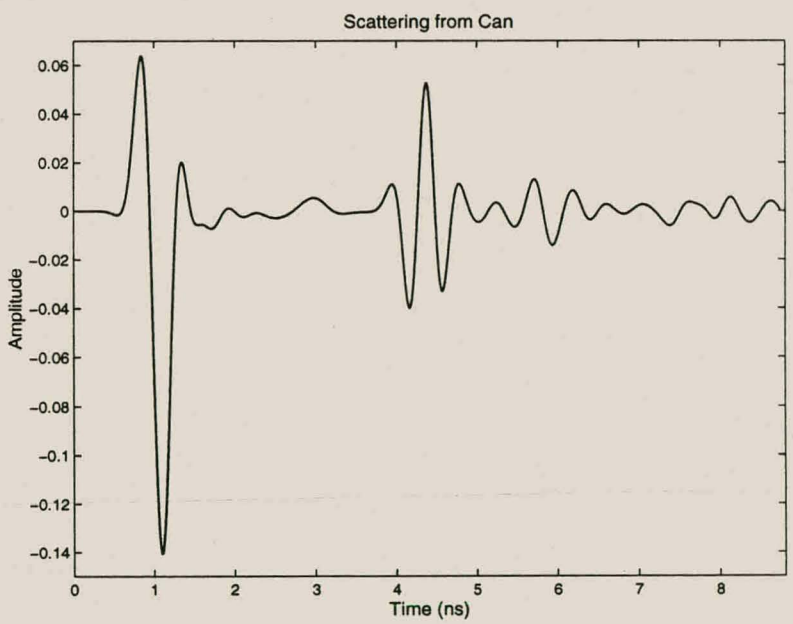

Figure 6.5: A-scan for a Superimposed Can and Soil Layer.

6.3 Natural Resonance Estimation

The late-time scattered field of a target can be represented as the sum of natural resonance modes. As discussed above the natural frequencies of a target are a function of its size and shape, therefore, a full description of those natural responses should be unique to a specific target and provides a potential basis for identification [34].

6.3.1 Linear Predictive Coding

Linear predictive filtering is used to estimate the returned signal as an *Auto-Regressive* (AR) process. The AR linear filter for generating the random process $x(n)$ (the returned scattered signal) from a white noise process with power spectral density σ_w^2 is

$$H(z) = \frac{1}{A(z)} = \frac{1}{1 + \sum_{k=1}^{p} a_k z^{-k}} \tag{6.1}$$

where a_k are the filter coefficients that determine the location of the poles of $H(z)$. These coefficients are related to the autocorrelation estimate $\gamma_{xx}(m) = E[x(n)x^*(n-m)]$ of the signal by

$$\gamma_{xx}(m) = \begin{cases} -\sum_{k=1}^{p} a_k \gamma_{xx}(m-k) & m > 0 \\ -\sum_{k=1}^{p} a_k \gamma_{xx}(m-k) + \sigma_w^2 & m = 0 \\ \gamma_{xx}^*(-m) & m < 0 \end{cases} \tag{6.2}$$

These are the *Yule-Walker* equations and can be expressed in matrix form and solved for by exploiting its Toeplitz symmetry.

$$\begin{bmatrix} \gamma_{xx}(0) & \gamma_{xx}(-1) & \gamma_{xx}(-2) & \cdots & \gamma_{xx}(-p) \\ \gamma_{xx}(1) & \gamma_{xx}(0) & \gamma_{xx}(-1) & \cdots & \gamma_{xx}(-p+1) \\ \vdots & \vdots & \vdots & & \vdots \\ \gamma_{xx}(p) & \gamma_{xx}(p-1) & \gamma_{xx}(p-2) & \cdots & \gamma_{xx}(0) \end{bmatrix} \begin{bmatrix} 1 \\ a_1 \\ \vdots \\ a_p \end{bmatrix} = \begin{bmatrix} \sigma_w^2 \\ 0 \\ \vdots \\ 0 \end{bmatrix} \tag{6.3}$$

Forward Linear Predictive Coding (LPC) is used to calculate the AR coefficients, a_k.

All-pole lattice filter implementations of equation (6.1) are widely used in seismology where the K_m reflection coefficients used in the implementation are identical to the reflection coefficients associated with the physical medium [6]. The Levinson-Durbin recursive algorithm is used to obtain the reflection coefficients, K_m, for the optimum lattice prediction filter.

$$a_m(m) = a_{m-1}(k) + K_m a^*_{m-1}(m-k) \qquad \begin{matrix} k = 1, 2, \ldots, m-1 \\ m = 1, 2, \ldots, p \end{matrix} \tag{6.4}$$

The reflection coefficients so obtained are used as the feature vectors describing the natural resonances of the system for detection purposes.

6.3.2 Implementation

6.3.2.1 Resampling and Filtering

Each BOR FDTD simulation has a different associated temporal time step, Δt that is problem specific. From a signal processing point of view, this time discretisation is generally way above the Nyquist limit for the specified -10dB bandwidth of 230MHz-2.2GHz (Chapter 4.2). Each scattered signal is resampled to a normalised sampling frequency of 10GHz

in order for the reflection coefficients, obtained in the LPC extraction, to be comparable across all the simulations.

A frequency domain plot for a PMN2 plastic mine return is shown in figure 6.6. The solid-line plot shows that significant resonances still exist outside the chosen representative bandwidth of 230MHz-2.2GHz. There is also a significant DC component that stems from the non-physical source treatment [22]. The resampled data is thus bandpass filtered through a FIR filter set to the incident pulse bandwidth to remove any undesired frequency components still present in the signal.

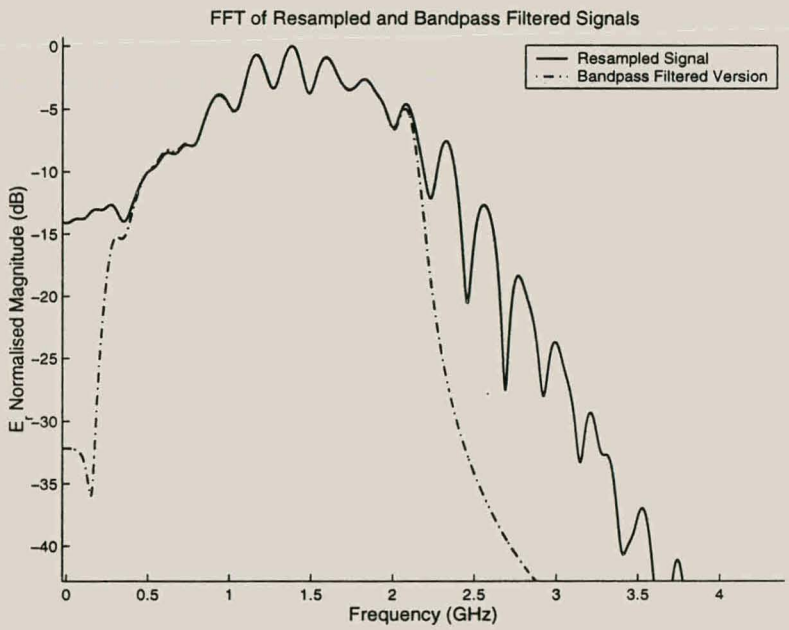

Figure 6.6: Resampled and Bandpass Filtered Return from PMN2 Mine.

6.3.2.2 AR Filter Order

The higher the order, p, of the AR filter in equation (6.1) the more accurately the AR estimate will reconstruct the original scattered signal. Figure 6.7 shows the reconstructed frequency domain plots of the signal for different filter orders compared to the original FFT of the signal. This figure shows how the AR filter poles *lock on* to the natural resonances

of the signal. The $p = 64$ order filter (dotted curve) has more poles than there are signal resonances to estimate and consequently tries to reproduce the bandpass filter zeros at the lower frequencies around 230MHz.

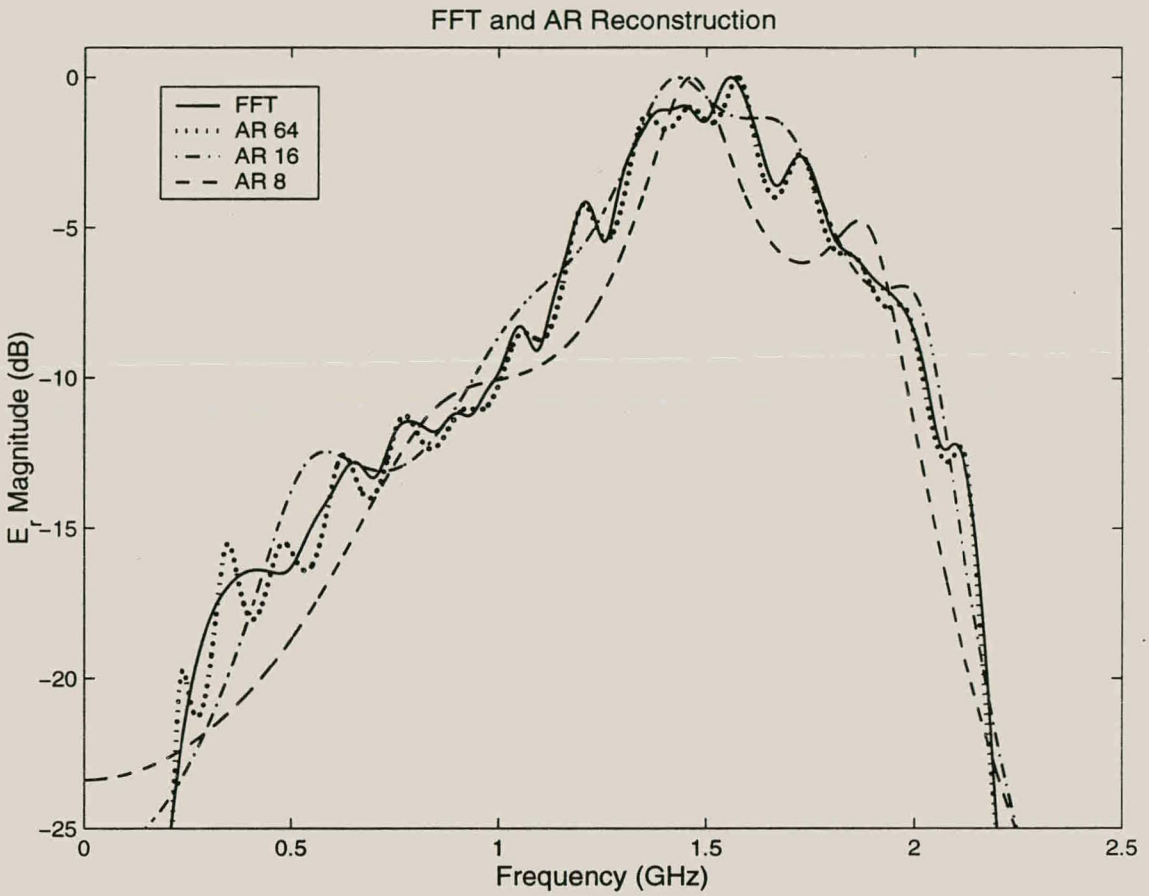

Figure 6.7: AR Filter Reconstruction.

The AR filter order is also related to the length of the autocorrelation estimate's (γ_{xx}) window size, m. The width of this window is an important parameter since the estimated reflection coefficients of the signal will depend on the amount of information computed within the window. A short window will only extract resonance information at localised regions as depicted in figure 6.8. A wider window, as in figure 6.9, will tend to include more effects from the interactions between different scattering objects. The resampled data is typically on the order of only a few hundred data points, making relatively wide autocorrelation windows feasible.

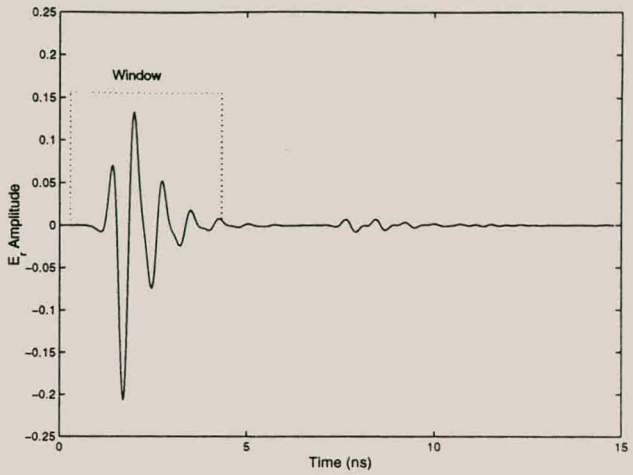

Figure 6.8: Short Correlation Window Length.

Figure 6.9: Wide Correlation Window Length.

Increasing the order of the AR filter will, however, make the estimated system more prone to noise. As thermal receiver noise [1] increases, more spurious peaks become present and the poles of the AR filter will experience difficulty estimating the correct poles of the signal. Figure 6.10 shows how different ordered AR filters handle thermal noise. The solid line is an accurate reconstruction for a SNR of 50dB. The higher order AR filters clearly are more prone to estimating spurious peaks.

[1] Thermal receiver noise is modelled as additive white Gaussian noise.

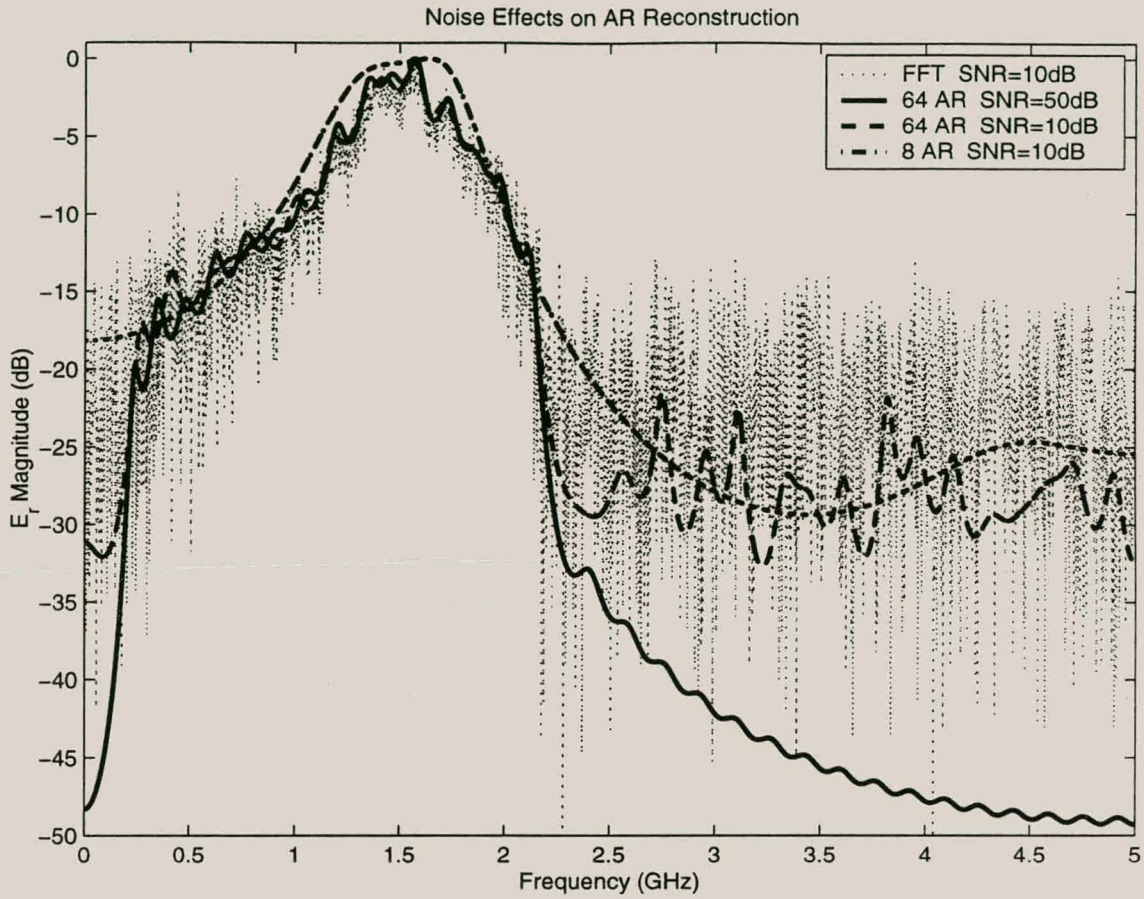

Figure 6.10: AR Reconstruction for Different SNR's.

6.4 Conclusion

The natural resonances present within a scattered signal can be estimated using linear predictive filtering. Reflection coefficients are determined that define a lattice filter implementation of an AR filter using the Levinson-Durbin recursion algorithm. Reflection coefficients are used, as opposed to straight AR coefficients, as feature vectors describing the model since they model more accurately the physical system [6]. Noise effects, filter order considerations and a qualitative discussion are all covered in this chapter so that the results of an identification process can be more readily analysed in terms of the physical system.

Chapter 7

Detection Results

7.1 Data Sets

The data generated by the BOR FDTD, as described in Chapter 5, is comprised of seven classes. Three of the classes describe typical clutter conditions:

- Stratified soil layers with no target scatterer present
- Rocks, modelled as spheres, of different dielectric properties and sizes
- Metallic beverage cans

The remaining four classes describe typical land-mine targets

- Large M20 metallic anti-tank mine
- Shallow-buried metallic Valmara59
- Plastic PMN2 anti-personnel mine

- Small plastic R2M2 mine

The generated data is divided into independent training, testing and validation data sets. The training and testing data sets are to be used together to optimise a detection procedure. Once a suitable detector has been trained and tested, it is validated using the validation data set. Only the scores from this latter validation phase are reproduced in this chapter. Table 7.1 shows how the generated data is split into the three sets.

	Nothing	Rock	Can	M20	V59	PMN2	R2M2
Train	52	136	150	97	137	146	150
Test	47	87	92	72	105	117	107
Val	52	92	112	86	113	114	118

Table 7.1: Training, Testing and Validation Data Sets

7.2 Method

Artificial Neural Networks (ANN's) are used to generate detection scores for three different classification problems.

- Firstly, detection is performed on a *per class* basis and the scores are used to decide upon the best ANN model to proceed with. This stage should give the most insight as to how well each target class compares and where the data becomes separable.
- Secondly, detection is performed on a *mine-no-mine* basis where the non-mine classes are lumped together against the mine classes in a binary decision test. This stage should give a rough idea of the overall detectability of the model for an arbitrary mine type.

- Lastly, detection is performed on a *selected* set of classes that are reasonably separable from each other and the ground clutter. This stage should, obviously, give the best scores and further investigations are performed here on the susceptibility of the model to increasing thermal receiver noise.

The scores presented in this chapter will typically be presented in the form of confusion matrices. Each cell of the matrix contains a total count of how many the input class feature vectors, specified by the row position, are classified as a specific estimated class, specified by the column position. In other words, the rows are the inputs and the column are the outputs of the detector. The total *probability of correctness* can be obtained by dividing the scores along the main diagonal [1] by the total number of feature vectors in the validation set.

The Signal to thermal receiver Noise Ratios (SNR) used in certain discussion in this chapter are generated by adding Gaussian white noise to the scattered time signal. The signal power term is taken as the average power across all the BOR FDTD simulations. In this way, data for a given SNR can be simply generated by adding the correct noise process.

7.3 Artificial Neural Networks

A standard back-propagation training algorithm is used on single hidden layer networks. A three layer ANN (input layer, hidden layer and output layer) can theoretically separate any, possibly unbounded convex region in the space spanned by the outputs. These convex regions have as many sides as there are nodes in the hidden layer [35].

The procedure for choosing the number of nodes in the hidden layer is traditionally taken as the square root of the product of the input and output layers. This is a very debatable

[1] This diagonal is highlighted in the results

issue though [36]. The number of hidden layers is taken as 10 for the detection problems discussed in this chapter. Numerous arbitrary configurations were computed for different RC feature vector orders with little difference in validation scores. These results are not truly pertinent to the design objective and will consequently not be reproduced.

All the ANN computations are generated using the Stuttgart Neural Network Simulator V4.2. [37].

7.4 Per-Class Detection

Firstly, the order of the RC feature vectors (which is the same as the order of the AR filter described in Chapter 6) needs to be chosen before further investigations are pursued. Table 7.2 shows the results obtained for a three layer network with 10 nodes in its hidden layer.

RC Order	6	8	16	20	32	64	128
Prob. Corr.	37.94%	39.85%	43.7%	47.2%	48.0%	50.2%	45.5%

Table 7.2: Per-Class Detection: Choice of RC Lattice Filter Order

With 128 order RC feature vectors, the ANN's performance starts to decrease as well become computationally expensive. This decrease in performance is believed to be attributed to the fact that the all-pole prediction filter tries to estimate the poles of the bandpass filter (as in figure 6.7) as well as any other spurious resonances outside of the incident field's -10dB bandwidth. The best results appear to be obtained with a RC filter order of 64. $p = 64$ still allows a reasonably sized autocorrelation window, after the signal has been resampled, for more accurate estimates.

The confusion matrices for an ANN with 64 inputs, 7 outputs and 10 nodes in a single

hidden layer are given in tables 7.4, 7.5 and 7.6 for signal-to-noise ratios of 20dB, 10dB and 5dB's respectively. The *nothing* label here pertains to the case where no scatterer is present in the model. The probabilities for correctness vs SNR are shown in table 7.3.

SNR	5dB	10dB	20dB
Prob. Corr.	32.9%	46.3%	56.6%

Table 7.3: Per-Class Detection: Pc vs SNR

	Estimated As							
Target	Nothing	Rock	Can	M20	V59	PMN2	R2M2	**Row Total**
Nothing	**0**	1	7	0	8	2	34	52
Rock	1	**34**	1	10	9	15	23	92
Can	0	7	**27**	1	24	20	33	112
M20	0	13	0	**53**	2	16	2	86
V59	0	4	12	0	**57**	17	23	113
PMN2	0	12	4	2	9	**81**	6	114
R2M2	0	3	21	0	9	4	**80**	118

Table 7.4: Per-Class Detection: 64th Order RC, SNR=20dB, Pc=56.6%

From these tables, the ANN struggles to classify the no-scatterer case under any conditions. This is understandable in a way since all the other classes contain the same information pertaining to ground conditions as does the no-scatterer class, which is purely comprised of ground information. The four individual land-mines classify very well, the weakest results of the four pertaining to the Valmara59 mine. The rock class is expected to have its estimated values distributed amongst the other classes. This is because it is modelled for a variety of different compositions and sizes and should have its RC's spread throughout the entire problem space. The biggest problem appears to be the R2M2 mine class. Its RC data appears to lie very close to the can and the no-scatterer classes, probably because of its small size. The ANN, when faced with such inseparable data, will have to place its hyper-planes in favour of one of the classes. It appears to do this in favour of the class which

	Estimated As							
Target	Nothing	Rock	Can	M20	V59	PMN2	R2M2	**Row Total**
Nothing	**0**	0	8	0	7	5	32	52
Rock	0	**24**	7	2	5	31	23	92
Can	1	2	**32**	0	16	10	51	112
M20	0	8	0	**54**	4	19	1	86
V59	0	3	21	1	**47**	22	19	113
PMN2	0	8	2	0	9	**89**	6	114
R2M2	0	4	17	0	17	8	**72**	118

Table 7.5: Per-Class Detection: 64th Order RC, SNR=10dB, Pc=46.3%

	Estimated As							
Target	Nothing	Rock	Can	M20	V59	PMN2	R2M2	**Row Total**
Nothing	**0**	0	13	2	10	13	14	52
Rock	0	**3**	12	7	5	46	19	92
Can	0	0	**29**	2	15	25	41	112
M20	0	0	1	**71**	2	9	3	86
V59	0	0	27	5	**20**	36	25	113
PMN2	0	1	9	9	12	**66**	17	114
R2M2	0	0	43	1	20	17	**37**	118

Table 7.6: Per-Class Detection: 64th Order RC, SNR=5dB, Pc=32.9%

carries the most information.

As the SNR decreases the probability of correctness decreases as expected. The influence of thermal noise appears to affect the Valmara59 class the most as can be seen from table 7.6.

7.5 Mine-no-Mine Detection

This stage uses exactly the same data as the *per-class* detection stage , only the ANN is now expected to train around the mines collectively and not individually. Four different ANN configurations were tested on this data and are depicted in tables 7.7 to 7.10.

	Estimated As		
Target	Mine	No Mine	**Row Total**
Mine	**358**	67	425
No Mine	179	**76**	255

Table 7.7: Mine-no-Mine Detection: Confusion Matrix for 32nd Order RC, 5 Nodes

	Estimated As		
Target	Mine	No Mine	**Row Total**
Mine	**386**	39	425
No Mine	206	**49**	255

Table 7.8: Mine-no-Mine Detection: Confusion Matrix for 32nd Order RC, 10 Nodes

	Estimated As		
Target	Mine	No Mine	**Row Total**
Mine	**376**	49	425
No Mine	196	**59**	255

Table 7.9: Mine-no-Mine Detection: Confusion Matrix for 16th Order RC, 5 Nodes

	Estimated As		
Target	Mine	No Mine	**Row Total**
Mine	**378**	47	425
No Mine	199	**56**	255

Table 7.10: Mine-no-Mine Detection: Confusion Matrix for 16th Order RC, 10 Nodes

Interestingly, the results are all very similar, with probabilities of correctness of about 63.8% for each. This merely confirms the discussion in the previous section, being that the mines classify very well individually as opposed to the clutter.

7.6 Selected-Class Detection

A *selected class* data set of the two most separable land-mines is taken from the original ensemble. The remainder of the selected set is comprised of the rock class and the no-scatterer class. The same ANN as for the *per-class* detection stage is used here and the results are computed for increasing thermal receiver noise. Tables 7.6 to 7.16 show the results for SNR's of 20dB, 10dB, 5dB, 2dB and 1dB respectively and table 7.11 shows the scores vs SNR values.

SNR	20dB	10dB	5dB	2dB	1dB
Prob. Corr.	70.9%	61.6%	50.9%	48.6%	48.3%

Table 7.11: Per-Class Detection: Pc vs SNR

	Estimated As				
Target	Nothing	Rock	M20	PMN2	**Row Total**
Nothing	**29**	16	1	6	52
Rock	14	**40**	11	27	92
M20	0	15	**64**	7	86
PMN2	1	9	3	**101**	114

Table 7.12: Selected-Class Detection: Confusion Matrix for 64th order RC, SNR=20dB

The probabilities of correctness for each of these problems follows the expected trend. The most significant result here is in table 7.6. Having removed the R2M2, can and Valmara59 classes from the problem, the ANN is now able to classify the no-scatterer class correctly. This result confirms the assumptions made in section 7.4 about the misclassification of the can and R2M2 classes. However, as the thermal receiver noise increases, the detection score on the no-scatterer class drops radically and the ANN chooses in favour of the PMN2 mine.

	Estimated As				
Target	Nothing	Rock	M20	PMN2	**Row Total**
Nothing	**21**	23	0	8	52
Rock	8	**33**	5	49	92
M20	2	7	**62**	15	86
PMN2	2	15	1	**96**	114

Table 7.13: Selected-Class Detection: Confusion Matrix for 64th order RC, SNR=10dB

	Estimated As				
Target	Nothing	Rock	M20	PMN2	**Row Total**
Nothing	**1**	16	0	35	52
Rock	3	**16**	7	66	92
M20	1	2	**65**	18	86
PMN2	2	13	6	**93**	114

Table 7.14: Selected-Class Detection: Confusion Matrix for 64th order RC, SNR=5dB

	Estimated As				
Target	Nothing	Rock	M20	PMN2	**Row Total**
Nothing	**0**	27	5	20	52
Rock	0	**43**	10	39	92
M20	0	10	**65**	11	86
PMN2	0	37	18	**59**	114

Table 7.15: Selected-Class Detection: Confusion Matrix for 64th order RC, SNR=2dB

	Estimated As				
Target	Nothing	Rock	M20	PMN2	**Row Total**
Nothing	**1**	9	3	39	52
Rock	0	**7**	11	74	92
M20	1	6	**66**	13	86
PMN2	0	9	13	**92**	114

Table 7.16: Selected-Class Detection: Confusion Matrix for 64th order RC, SNR=1dB

7.7 Conclusion

The individual land-mines generate good detectability scores in general. The false alarm rate will, however, be quite high for the no-scatterer, rock and can classes as can be deduced from the confusion matrices in section 7.5. The reasoning here is that for classes that appear to be inseparable in the input space, the ANN cannot place any hyper-planes through the data region optimally and, instead, places it in favour of the class that contains the most information. This is confirmed by the results in table 7.6 where, in the absence of the confusing R2M2 and can classes, the ANN classified the no-scatterer class with better accuracy than before.

The results here are not entirely favourable from a mine detection point of view because of the probability of false alarm. The individual land-mines are quite separable from each other, however, to establish how well they stand out against ground clutter, a more complete model needs to be generated that includes a wider range of clutter types.

Chapter 8

Conclusion

8.1 Summary

In this thesis, a Body-of-Revolution Finite-Difference Time-Domain method formulation has been developed for the modelling of scattered Ground Penetrating Radar return signals off buried rotationally symmetric land-mines. The formulation is designed around a wideband incident field bandwidth of 230MHz to 2.2GHz. The formulation runs orders of magnitude faster than the three dimensional FDTD counterpart and uses significantly less system resources. The BOR FDTD simulator runs effectively on Pentium II processors with at least 64Mbytes of RAM. The formulation is validated using known spherical scattering algorithms and by checking for the correct wave propagation speeds within different media.

Models are generated that simulate real world conditions as accurately as possible without adding too much complexity to the formulation. Rough air-ground interfaces, stratified soil layers, lossy dielectric soil conditions and arbitrary rotationally symmetric geometries can all be inserted into the simulation with relative ease. A data set that models a wide variety of combinations of such conditions is generated and divided into a training, testing and

validation set, ready for post-processing.

Reflection Coefficients that model real world phenomena more accurately than straight Auto-Regressive coefficients are determined from the data sets using Linear Predictive Coding. These RC's are used as feature vectors for training, testing and validating simple Artificial Neural Networks modelled with a standard back-propagation training algorithm. The results are analysed by observing the confusion matrices obtained from various networks with additive thermal receiver noise.

8.2 Results

The land-mines chosen are simplistic models but do separate to a certain extent from each other and from ground clutter, even in the presence of low signal to thermal receiver noise ratios. The smaller R2M2 mine was found to significantly confuse the detection of the clutter class, probably owing to its size. This was validated by applying the detection process on a selected subset of target scatterers.

The overall result for all seven classes approaches 50% while a binary test for the presence of a mine or no-mine sits comfortable at 63% for a range of different ANN's and order AR predictive filters. The selected *well behaved* classes for high SNR values approaches 70%. Overall, the results are encouraging but not favourable. From the generated confusion matrices, the chosen land-mines appear to be reasonably *individually* separable. They are not, however, so separable from the ground and clutter models. The data model should be extended, however, to include more clutter types in order to obtain a better estimate of how well the land-mines are separable from typical clutter conditions.

8.3 Future Work

The current absorbing boundary condition treatments, needed to reduce reflections from the edges of the FDTD domain, need to be improved upon to increase the overall accuracy of the simulator. An optimised PML should perhaps be investigated in depth.

A larger and more representative data set should be generated for pattern recognition purposes. This will increase the accuracy of the model from a real world perspective but will take a lot more information concerning clutter types into account.

A model containing soil layers is not necessarily essential when dealing with shallowly buried landmines. Furthermore, the digging process involved in burying the mines probably would destroy any surrounding soil layers. The model is, however, possibly useful for deeply buried unexploded ordinance.

Off-axis excitation is theoretically possible to model using the higher order Fourier modes in chapter 2 to model the source and update equations. This would permit B&C scans in addition to the on-axis data presented here.

Bibliography

[1] J.Trevelyan, "Technology transfer in humanitarian demining," in *Sec. Int. Conf. on the Detection of Abandoned Land-mines*, (Edinburgh), pp. 23–27, IEE, October 1998.

[2] J.M.Bourgeois and G.S.Smith, "A complete electromagnetic simulation of the seperated-apeture sensor for detecting buried land mines," *IEEE Trans. Antennas Propagat.*, vol. 46, pp. 1419–1426, October 1998.

[3] D.E.Merewether and R.Fisher, "Finite difference solution of Maxwell's equations for E.M.P. applications," Tech. Rep. EMA-79-R-4, Defense Nuclear Agency, Washington, D.C., 1980.

[4] D.B.Davidson and R.W.Ziolkowski, "Body-of-revolution finite-difference time-domain modelling of space-time focusing by a three dimensional lens," *J. Optical Soc. Am.*, vol. 11, pp. 1471–1490, April 1994.

[5] A.C.Dubey and R.L.Barnard, eds., *Detection and Remediation Technologies for Mines and Minelike Targets*, vol. 3079, (Orlando), SPIE, 1997.

[6] J.G.Proakis and D.G.Manolakis, *Digital Signal Processing: Principles, Algorithms and Applications*. Prentice-Hall, 3rd ed., 1996.

[7] S.Vitebskiy and L.Carin, "Ultra-wideband, short-pulse ground-penetrating radar: Simulation and measurement," *IEEE Trans. Geosci. Remote Sensing*, vol. 44, pp. 1575–1583, December 1996.

[8] W. Weedon and C. Rappaport, "A general method for FDTD modeling of wave propagation in arbitrary frequency-dispersive media," *IEEE Trans. Antennas Propagat.*, vol. 45, pp. 401–410, March 1997.

[9] M.Bingle, "The finite-difference time-domain modelling of liquids with dispersive dielectric properties," Master's thesis, Stellenbosch Univ., 1995.

[10] K.S.Yee, "Numerical solution of initial boundary value problems involving Maxwell's equations in isotropic media," *IEEE Trans. Antennas Propagat.*, vol. 14, pp. 302–307, March 1966.

[11] K.S.Kunz and R.J.Leubbers, *The Finite Difference Time Domain Method for Electromagnetics.* Boca Raton, FL: CRC Press, 1993.

[12] W. L. Stutzman and G. A. Thiele, *Antenna Theory and Design.* Wiley, second ed., 1998.

[13] W.C.Chew, *Waves and Fields in Inhomogenous Media.* New York: Van Nostrand Reinhold, 1990.

[14] R.Holland and J.W.Williams, "Total-field versus scattered-field finite difference codes: A comparative assessment.," *IEEE Trans. Nucl. Sci.*, vol. 30, no. 6, pp. 4583–4588, 1983.

[15] A.Taflove, *Computational Electrodynamics: The Finite-Difference Time-Domain Method.* Boston, MA: Artech House, 1995.

[16] G.S.Smith, *An Introduction to Classical Electromagnetic Radiation*, ch. 3.7.3. Cambridge Univ. Press, 1997.

[17] D.S.Katz, E.T.Thiele, and A.Taflove, "Validation and extension to three dimensions of the Berenger PML absorbing boundary condition for FDTD meshes," *IEEE Microwave Guided Wave Lett.*, vol. 4, pp. 268–270, August 1994.

[18] C.A.Balanis, *Advanced Engineering Electromagnetics.* New York: Wiley, 1989.

[19] R.F.Harrington, *Time-Harmonic Electromagnetic Fields.* New York: McGraw-Hill, 1961.

[20] F.Bowman, *Introduction to Bessel Functions.* London: Longmans, 1938.

[21] G.N.Watson, *A Treatise on the Theory of Bessel Functions.* Cambridge, England: Cambridge Univ. Press, 2nd ed., 1966.

[22] C.L.Wagner and J.B.Schneider, "Divergent fields, charge, and capacitance in FDTD simulations," *IEEE Trans. Microwave Theory Tech.*, vol. 46, pp. 2131–2136, December 1998.

[23] B.Sai, I.Morrow, and P. Genderen, "Limits of detection of buried landmines based on local echo contrasts," in *European Microwave Conference*, (Amsterdam), pp. 121–125, October 1998.

[24] D.J.Daniels, "Surface-penetrating radar," *Elect. Comm. Eng. Journal*, pp. 165–182, August 1996.

[25] E. Thorsos, "The validity of the Kirchhoff approximation for rough surface scattering using a Gaussian roughness spectrum," *J. Acoustic Soc. Am.*, vol. 83, pp. 72–98, January 1998.

[26] T. Dogaru and L. Carin, "Time-domain sensing of targets buried under a rough air-ground surface," *IEEE Trans. Antennas Propagat.*, vol. 46, pp. 360–372, March 1998.

[27] F. Hastings, J. Schneider, and S. Broschat, "A Monte-Carlo FDTD technique for rough surface scattering," *IEEE Trans. Antennas Propagat.*, vol. 43, pp. 1183–1191, November 1995.

[28] A. Papoulis, *Probability, Random Variables, and Stochastic Processes*. McGraw-Hill, 1991.

[29] K. O'Neill, R. Lussky, and K. Paulsen, "Scattering from a metallic object embedded near the randomly rough surface of a lossy dielectric," *IEEE Trans. Geosci. Remote Sensing*, vol. 34, pp. 367–376, March 1996.

[30] D.Wong and L.Carin, "Analysis and processing of ultra wide-band SAR imagery for buried land-mine detection," *IEEE Trans. Antennas Propagat.*, vol. 46, pp. 1747–1748, November 1998.

[31] U.S.A. Dept. of Defense, "Minefacts." CDROM. v1.2.

[32] L.Carin, N.Geng, M.McClure, J.Sichina, and L.Nguyen, "Ultra-wideband synthetic-aperture radar for mine-field detection," *IEEE Trans. Antennas Propagat.*, vol. 41, pp. 18–33, February 1999.

[33] D.J.Daniels, *Surface-penetrating Radar*. London: IEE, 1996.

[34] C.E.Baum, E.J.Rothwell, K.Chen, and D.P.Nyquist, "The Singularity Expansion Method and its application to target recognition," in *Proc. IEEE*, vol. 79, October 1991.

[35] R.P.Lippmann, "An introduction to computing with neural nets," *IEEE ASSP Magazine*, pp. 4–22, April 1987.

[36] J.M.Zurada, *Introduction to Artificial Neural Networks*. New York: West, 1992.

[37] Univ. Stuttgart, "Stuttgart Neural Network Simulator." ftp.informatik.uni-stuttgart.de/pub/SNNS.

[38] H.A.Haus and J.R.Melcher, *Electromagnetic Fields and Energy*. Prentice-Hall, 1989. Appendix 1.

[39] W.C.Chew and W.H.Weedon, "A 3D perfectly matched medium from modified Maxwell's equations with stretched coordinates," *Microwave Opt. Technol. Lett.*, vol. 7, pp. 599–604, September 1994.

[40] F.L.Texeira and W.C.Chew, "PML-FDTD in cylindrical and spherical grids," *IEEE Microwave Guided Wave Lett.*, vol. 7, pp. 285–287, September 1997.

Appendix A

Coordinate System Conversion

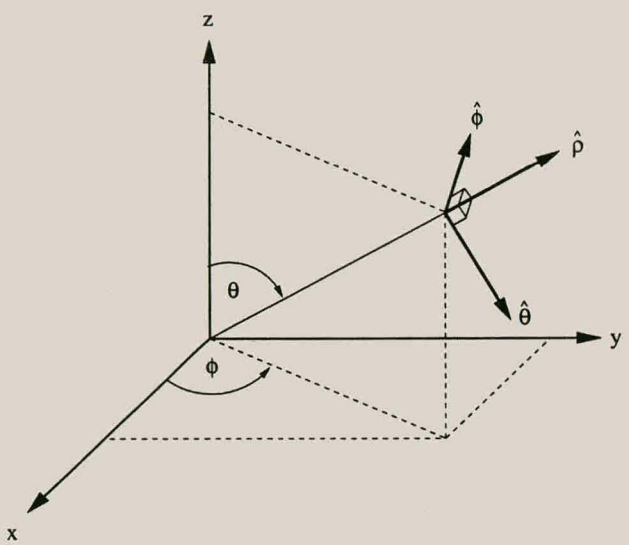

Figure A.1: Vector Conversion.

A Coordinate System Conversion

Cartesian - Spherical

$$\hat{x} = \hat{\rho}\sin\theta\cos\phi + \hat{\theta}\cos\theta\cos\phi - \hat{\phi}\sin\phi \quad (A.1)$$

$$\hat{y} = \hat{\rho}\sin\theta\sin\phi + \hat{\theta}\cos\theta\sin\phi + \hat{\phi}\cos\phi \quad (A.2)$$

$$\hat{z} = \hat{\rho}\cos\theta - \hat{\theta}\sin\theta \quad (A.3)$$

$$\hat{\rho} = \hat{x}\sin\theta\cos\phi + \hat{y}\sin\theta\sin\phi + \hat{z}\cos\theta \quad (A.4)$$

$$\hat{\theta} = \hat{x}\cos\theta\cos\phi + \hat{y}\cos\theta\sin\phi - \hat{z}\sin\theta \quad (A.5)$$

$$\hat{\phi} = -\hat{x}\sin\phi + \hat{y}\cos\phi \quad (A.6)$$

Cartesian - Cylindrical

$$\hat{x} = \hat{\rho}\cos\phi - \hat{\phi}\sin\phi \quad (A.7)$$

$$\hat{y} = \hat{\rho}\sin\phi + \hat{\phi}\cos\phi \quad (A.8)$$

$$\hat{z} = \hat{z} \quad (A.9)$$

$$\hat{\rho} = \hat{x}\cos\phi + \hat{y}\sin\phi \quad (A.10)$$

$$\hat{\phi} = -\hat{x}\sin\phi + \hat{y}\cos\phi \quad (A.11)$$

$$\hat{z} = \hat{z} \quad (A.12)$$

Source: Haus & Melcher [38]

Appendix B

Fourier Series

The Fourier series of an even function on the interval $(-p, p)$ is the **cosine series**.

$$f(x) = \frac{a_0}{2} + \sum_{k=1}^{\infty} a_k \cos\left(\frac{k\pi}{p}x\right) \tag{B.1}$$

where

$$a_0 = \frac{2}{p}\int_0^p f(x)dx \tag{B.2}$$

$$a_k = \frac{2}{p}\int_0^p f(x)\cos\left(\frac{k\pi}{p}x\right)dx \tag{B.3}$$

The Fourier series of an odd function on the interval $(-p, p)$ is the **sine series**.

$$f(x) = \sum_{k=1}^{\infty} b_k \sin\left(\frac{k\pi}{p}x\right) \tag{B.4}$$

where

$$b_k = \frac{2}{p}\int_0^p f(x)\sin\left(\frac{k\pi}{p}x\right)dx \tag{B.5}$$

Appendix C

Absorbing Boundary Conditions

The ABC derived here is based on the formulation in [13].

The one-way wave equation only admits solutions travelling in one direction and is used here to represent waves travelling in the positive or negative $f(z \mp ct)$ respectively.

$$\left[\frac{\partial}{\partial z} \mp \frac{1}{v}\frac{\partial}{\partial t}\right]\phi(z,t) = 0 \tag{C.1}$$

The wave needs to absorbed across the boundary, therefore :

$$\left.\frac{\partial}{\partial z}\phi(z,t)\right|_{z=\text{boundary}} = \pm\frac{1}{v}\left.\frac{\partial}{\partial t}\phi(z,t)\right|_{z=\text{boundary}} \tag{C.2}$$

Finite differencing is employed consistently with figure 3.2.

For the positively travelling wave :

$$\phi_0^{n+1} = \phi_0^n\left[\frac{1 - v\Delta t}{\Delta z}\right] + \phi_1^n\frac{v\Delta t}{\Delta z} \tag{C.3}$$

For the negatively travelling wave :

$$\phi^{n+1}_{z_{max}+1} = \phi^{n}_{z_{max}+1}\left[\frac{1-v\Delta t}{\Delta z}\right] + \phi^{n}_{z_{max}}\frac{v\Delta t}{\Delta z} \tag{C.4}$$

A wave travelling in the positive ρ direction will be treated in a similar manner as above. The one-way wave equation becomes

$$\left[\frac{\partial}{\partial \rho} + \frac{1}{v}\frac{\partial}{\partial t}\right]\phi(\rho, t) = 0 \tag{C.5}$$

which, when discretised, becomes

$$\phi^{n+1}_{\rho_{max}+1} = \phi^{n}_{\rho_{max}+1}\left[\frac{1-v\Delta t}{\Delta \rho}\right] + \phi^{n}_{\rho_{max}}\frac{v\Delta t}{\Delta \rho} \tag{C.6}$$

Appendix D

Body-of-Revolution Perfectly Matched Layer

The Berenger PML has become one of the most popular grid truncation schemes for use with the FDTD method. Recent work by Chew and Weedon [39] extended the original split field formulation to include complex coordinate stretching along the three Cartesian coordinates. The complex stretched coordinate approach has been extended to cylindrical and spherical coordinates [40]. The derivation presented here is for the specific BOR expanded FDTD formulation described in Chapter 3.

Assume the PML starts at $\rho > \rho_0$ and $z > z_0$. The complex spatial variables are defined for reflectionless absorption as [40]

$$\rho \to \hat{\rho} = \rho_0 + \int_{\rho_0}^{\rho} S_\rho(\rho')d\rho' \qquad \frac{\partial}{\partial\hat{\rho}} = \frac{1}{S_\rho}\frac{\partial}{\partial\rho} \tag{D.1}$$

$$z \to \hat{z} = z_0 + \int_{z_0}^{z} S_z(z')dz' \qquad \frac{\partial}{\partial\hat{z}} = \frac{1}{S_z}\frac{\partial}{\partial z} \tag{D.2}$$

where $S_\zeta(\zeta)$ are the complex stretching variables. A further degree of freedom is obtained

be defining

$$S_\rho(\rho') = 1 - j\frac{\sigma_\rho(\rho')}{\omega\epsilon_0} \tag{D.3}$$

$$S_z(z') = 1 - j\frac{\sigma_z(z')}{\omega\epsilon_0} \tag{D.4}$$

The modified frequency domain Maxwell's equations mapped into stretched coordinate space are given below.

$$j\omega\mu H_\rho = \frac{E_z}{\hat{\rho}} + \frac{\partial E_\phi}{\partial \hat{z}} \tag{D.5}$$

$$j\omega\mu H_\phi = \frac{\partial E_z}{\partial \hat{\rho}} - \frac{\partial E_\rho}{\partial \hat{z}} \tag{D.6}$$

$$j\omega\mu H_z = -\frac{1}{\hat{\rho}}\left[\frac{\partial(\hat{\rho}E_\phi)}{\partial \hat{\rho}} + E_\rho\right] \tag{D.7}$$

$$j\omega\epsilon E_\rho + \sigma E_\rho = \frac{H_z}{\hat{\rho}} - \frac{\partial H_\phi}{\partial \hat{z}} \tag{D.8}$$

$$j\omega\epsilon E_\phi + \sigma E_\phi = \frac{\partial H_\rho}{\partial \hat{z}} - \frac{\partial H_z}{\partial \hat{\rho}} \tag{D.9}$$

$$j\omega\epsilon E_z + \sigma E_z = \frac{1}{\hat{\rho}}\left[\frac{\partial(\hat{\rho}H_\phi)}{\partial \hat{\rho}} - H_\rho\right] \tag{D.10}$$

The partial derivatives can be mapped out using (D.1) and (D.2).

$$j\omega\mu H_\rho = \frac{E_z}{\hat{\rho}} + \frac{1}{S_z}\frac{\partial E_\phi}{\partial z} \tag{D.11}$$

$$j\omega\mu H_\phi = \frac{1}{S_\rho}\frac{\partial E_z}{\partial \rho} - \frac{1}{S_z}\frac{\partial E_\rho}{\partial z} \tag{D.12}$$

$$j\omega\mu H_z = -\frac{1}{\hat{\rho}}\left[\frac{1}{S_\rho}\frac{\partial(\hat{\rho}E_\phi)}{\partial \rho} + E_\rho\right] \tag{D.13}$$

$$j\omega\epsilon E_\rho + \sigma E_\rho = \frac{H_z}{\hat{\rho}} - \frac{1}{S_z}\frac{\partial H_\phi}{\partial z} \tag{D.14}$$

$$j\omega\epsilon E_\phi + \sigma E_\phi = \frac{1}{S_z}\frac{\partial H_\rho}{\partial z} - \frac{1}{S_\rho}\frac{\partial H_z}{\partial \rho} \tag{D.15}$$

$$j\omega\epsilon E_z + \sigma E_z = \frac{1}{\hat{\rho}}\left[\frac{1}{S_\rho}\frac{\partial(\hat{\rho}H_\phi)}{\partial \rho} - H_\rho\right] \tag{D.16}$$

Each of the above equations is modified so that neither S_ρ, S_z, $\hat{\rho}$ nor $\hat{z}$ appear in the denominator.

$$j\omega\mu S_z \frac{\hat{\rho}}{\rho} H_\rho = \frac{S_z E_z}{\rho} + \frac{\partial}{\partial z}\left(\frac{\hat{\rho}}{\rho} E_\phi\right) \tag{D.17}$$

$$j\omega\mu S_z S_\rho H_\phi = \frac{\partial S_z E_z}{\partial \rho} - \frac{\partial S_\rho E_\rho}{\partial z} \tag{D.18}$$

$$j\omega\mu S_\rho \frac{\hat{\rho}}{\rho} H_z = -\frac{1}{\rho}\frac{\partial(\hat{\rho} E_\phi)}{\partial \rho} - \frac{S_\rho E_\rho}{\rho} \tag{D.19}$$

$$j\omega\epsilon S_z \frac{\hat{\rho}}{\rho} E_\rho + \sigma S_z \frac{\hat{\rho}}{\rho} E_\rho = \frac{S_z H_z}{\hat{\rho}} - \frac{\partial}{\partial z}\left(\frac{\hat{\rho}}{\rho} H_\phi\right) \tag{D.20}$$

$$j\omega\epsilon S_z S_\rho E_\phi + \sigma S_z S_\rho E_\phi = \frac{\partial S_\rho H_\rho}{\partial z} - \frac{\partial S_z H_z}{\partial \rho} \tag{D.21}$$

$$j\omega\epsilon S_\rho \frac{\hat{\rho}}{\rho} E_z + \sigma S_\rho \frac{\hat{\rho}}{\rho} E_z = \frac{1}{\rho}\frac{\partial(\hat{\rho} H_\phi)}{\partial \rho} - \frac{S_\rho H_\rho}{\rho} \tag{D.22}$$

The fields are normalised with respect to their stretched coordinates.

$$E'_\rho = S_\rho E_\rho \qquad H'_\rho = S_\rho H_\rho$$
$$E'_\phi = \frac{\hat{\rho}}{\rho} E_\phi \qquad H'_\phi = \frac{\hat{\rho}}{\rho} H_\phi$$
$$E'_z = S_z E_z \qquad H'_z = S_z H_z$$

The equations expressed in terms of these normalised fields become

$$j\omega\mu \frac{S_z \hat{\rho}}{S_\rho \rho} H'_\rho = \frac{E'_z}{\rho} + \frac{\partial E'_\phi}{\partial z} \tag{D.23}$$

$$j\omega\mu \frac{S_z S_\rho \rho}{\hat{\rho}} H'_\phi = \frac{\partial E'_z}{\partial \rho} - \frac{\partial E'_\rho}{\partial z} \tag{D.24}$$

$$j\omega\mu \frac{S_\rho \hat{\rho}}{S_z \rho} H'_z = -\frac{\partial E'_\phi}{\partial \rho} - \frac{E'_\rho}{\rho} \tag{D.25}$$

$$[j\omega\epsilon + \sigma] \frac{S_z \hat{\rho}}{S_\rho \rho} E'_\rho = \frac{H'_z}{\rho} - \frac{\partial H'_\phi}{\partial z} \tag{D.26}$$

$$[j\omega\epsilon + \sigma] \frac{S_z S_\rho \rho}{\hat{\rho}} E'_\phi = \frac{\partial H'_z}{\partial \rho} - \frac{\partial H'_\rho}{\partial z} \tag{D.27}$$

$$[j\omega\epsilon + \sigma] \frac{S_\rho \hat{\rho}}{S_z \rho} E'_z = \frac{1}{\rho}\frac{\partial \rho H'_\phi}{\partial \rho} - \frac{H'_\rho}{\rho} \tag{D.28}$$

The above equations need to be *unpacked* further by defining

$$P_\rho = \frac{\hat{\rho}}{S_\rho \rho} E'\rho \qquad P_\phi = \frac{S_z \rho}{\hat{\rho}} E'\phi \qquad P_z = \frac{\hat{\rho}}{S_z \rho} E'_z$$

$$Q_\rho = \frac{\hat{\rho}}{S_\rho \rho} H'\rho \qquad Q_\phi = \frac{S_z \rho}{\hat{\rho}} H'\phi \qquad Q_z = \frac{\hat{\rho}}{S_z \rho} H'_z$$

$$P'_\rho = S_z P_\rho \qquad P'_\phi = S_\rho P_\phi \qquad P'_z = S_z P_z$$

Equations (D.23- D.28) are expressed in terms of **P** and **Q** yielding

$$j\omega\mu S_z Q_\rho = \frac{E'_z}{\rho} + \frac{\partial E'_\phi}{\partial z} \tag{D.29}$$

$$j\omega\mu S_\rho Q_\phi = \frac{\partial E'_z}{\partial \rho} - \frac{\partial E'_\rho}{\partial z} \tag{D.30}$$

$$j\omega\mu S_\rho Q_z = -\frac{\partial E'_\phi}{\partial \rho} - \frac{E'_\rho}{\rho} \tag{D.31}$$

$$[j\omega\epsilon + \sigma] P'_\rho = \frac{H'_z}{\rho} - \frac{\partial H'_\phi}{\partial z} \tag{D.32}$$

$$[j\omega\epsilon + \sigma] P'_\phi = \frac{\partial H'_z}{\partial \rho} - \frac{\partial H'_\rho}{\partial z} \tag{D.33}$$

$$[j\omega\epsilon + \sigma] P'_z = \frac{1}{\rho}\frac{\partial \rho H'_\phi}{\partial \rho} - \frac{H'_\rho}{\rho} \tag{D.34}$$

An additional set of updates needs to be computed to solve for $\mathbf{P}'$. Using equations (D.3) and (D.4), the additional updates in the time domain can be expressed as

$$\frac{\partial}{\partial t}\begin{bmatrix} P'_\rho \\ P'_\phi \\ P'_z \end{bmatrix} = \frac{\partial}{\partial t}\begin{bmatrix} P_\rho \\ P_\phi \\ P_z \end{bmatrix} + \frac{1}{\epsilon_0}\begin{bmatrix} \sigma_z & 0 & 0 \\ 0 & \sigma_\rho & 0 \\ 0 & 0 & \sigma_\rho \end{bmatrix}\begin{bmatrix} P_\rho \\ P_\phi \\ P_z \end{bmatrix} \tag{D.35}$$

A last set of updates is required to solve for $\mathbf{P}$ in terms of $\mathbf{E}'$. Again using equations (D.3)

and (D.4) and remembering that

$$\hat{\rho} = \begin{cases} \rho & \rho < \rho_0 \\ \rho - \frac{j}{\omega\epsilon_0}\int_{\rho_o}^{\rho} \sigma_\rho(\rho')d\rho' & \rho > \rho_0 \end{cases}$$

these updates can be expressed in the time domain as

$$\frac{\partial P_\rho}{\partial t} + \frac{\sigma_\rho}{\epsilon_0}P_\rho = \frac{\partial E_\rho}{\partial t} + \frac{1}{\rho\epsilon_0}\left[\int_{\rho_o}^{\rho}\sigma_\rho(\rho')d\rho'\right]E_\rho \quad \text{(D.36)}$$

$$\frac{\partial P_\phi}{\partial t} + \frac{1}{\rho\epsilon_0}\left[\int_{\rho_o}^{\rho}\sigma_\rho(\rho')d\rho'\right]P_\phi = \frac{\partial E_\phi}{\partial t} + \frac{\sigma_z}{\epsilon_0}E_\phi \quad \text{(D.37)}$$

$$\frac{\partial P_z}{\partial t} + \frac{\sigma_z}{\epsilon_0}P_z = \frac{\partial E_z}{\partial t} + \frac{1}{\rho\epsilon_0}\left[\int_{\rho_o}^{\rho}\sigma_\rho(\rho')d\rho'\right]E_z \quad \text{(D.38)}$$

There are thus three sets of update equations that need to be computed in order to solve for the BOR PML formulation. The final set (D.36-D.37) is dependent on the radial starting point of the PML region (ρ_0) and of the configuration of the absorbing medium therein. Each FDTD simulation that utilises a different grid setup will therefore have to have its PML region re-optimised. Unfortunately, little work has been done to date on efficient optimisation of the radially dependent PML region.

Appendix E

Spherical Wave Functions

E.1 Method of Separation of Variables in Spherical Coordinates

The method of separation of variables is used extensively for finding solutions to the cylindrical and spherical Helmholtz equations. In spherical coordinates the Helmholtz equation (E.1) is

$$\frac{1}{r^2}\frac{\partial}{\partial r}\left(r^2\frac{\partial \psi}{\partial r}\right) + \frac{1}{r^2\sin\theta}\frac{\partial}{\partial \theta}\left(\sin\theta\frac{\partial \psi}{\partial \theta}\right) + \frac{1}{r^2\sin^2\theta}\frac{\partial^2\psi}{\partial \phi^2} + k^2\psi = 0 \qquad \text{(E.1)}$$

where $k = \omega\sqrt{\mu\epsilon}$ is the phase constant. Using the method of separation of variables and letting $\psi = R(r)H(\theta)\Phi(\phi)$, a set of separated equations is obtained.

$$\frac{d}{dr}\left(r^2\frac{dR}{dr}\right) + [(kr)^2 - n(n+1)]R = 0 \qquad \text{(E.2)}$$

$$\frac{1}{\sin\theta}\frac{d}{d\theta}\left(\sin\theta\frac{dH}{d\theta}\right) + \left[n(n+1) - \frac{m^2}{\sin^2\theta}\right]H = 0 \qquad \text{(E.3)}$$

$$\frac{d^2\Phi}{d\phi^2} + m^2\Phi = 0 \qquad \text{(E.4)}$$

Wave Type	Wave Functions	Zeroes	Poles
Travelling wave $(-r)$	$h_n^{(1)}(kr) = j_n(kr) + jy_n(kr)$	$kr \to j\infty$	$kr = 0$ $kr \to -j\infty$
Travelling wave $(+r)$	$h_n^{(2)}(kr) = j_n(kr) - jy_n(kr)$	$kr \to -j\infty$	$kr = 0$ $kr \to j\infty$
Standing wave	$j_n(kr)$ for $\pm r$	Infinite	$kr \to \pm\infty$
Standing wave	$y_n(kr)$ for $\pm r$	Infinite	$kr = 0$ $kr \to \pm\infty$

Table E.1: Wave Functions, Zeroes and Poles for Radial Waves in Spherical Coordinates.

Solutions to (E.2) are of the form

$$R_1(r) = A_1 j_n(kr) + B_1 y_n(kr) \quad \text{or} \quad R_2(r) = C_1 h_n^{(1)}(kr) + D_1 h_n^{(2)}(kr) \tag{E.5}$$

where $j_n(kr)$ and $y_n(kr)$ are *spherical Bessel functions* of the first and second kind respectively. They are used to represent radial standing waves. $h_n^{(1)}(kr)$ and $h_n^{(2)}(kr)$ are *spherical Hankel functions* of the first and second kind respectively. They represent radial travelling waves. The spherical Bessel functions are related to the regular Bessel functions by

$$z_n(kr) = \sqrt{\frac{\pi}{2kr}} Z_{n+1/2}(kr)$$

Table E.1 [1] shows the wave functions used to represent radial standing and travelling waves.

The solutions to (E.3) are of the form

$$\begin{aligned} H_1(\theta) &= A_2 P_n^m(\cos\theta) + B_2 P_n^m(-\cos\theta) \quad n \neq \text{integer} \quad \text{or} \\ H_2(\theta) &= C_2 P_n^m(\cos\theta) + D_2 Q_n^m(\cos\theta) \quad n = \text{integer} \end{aligned} \tag{E.6}$$

where P_n^m and Q_n^m are *associated Legendre functions* of the first and second kind respec-

[1] reproduced from [18]

tively.

The solutions to (E.4) are simply *harmonic functions*.

$$\Phi_1(\phi) = A_3 e^{-jm\phi} + B_3 e^{+jm\phi} \quad \text{or} \quad \Phi_2(\phi) = C_3 \cos(m\phi) + D_3 \sin(m\phi) \tag{E.7}$$

E.2 Construction of Solutions

In a homogeneous source free region, the field satisfies

$$-\nabla \times \mathbf{E} = j\omega\mu\mathbf{H} \qquad \nabla \cdot \mathbf{H} = 0$$
$$\nabla \times \mathbf{H} = j\omega\epsilon\mathbf{E} \qquad \nabla \cdot \mathbf{E} = 0$$

The divergenceless character of the fields allows us to describe them in terms of magnetic or electric vector potentials (**A** or **F** respectively). The electromagnetic fields, in terms of the superposition of these potentials, are given by [19]

$$\mathbf{E} = -\nabla \times \mathbf{F} + \frac{1}{j\omega\epsilon}(\nabla \times \nabla \times \mathbf{A}) \tag{E.8}$$

$$\mathbf{H} = \nabla \times \mathbf{A} + \frac{1}{j\omega\mu}(\nabla \times \nabla \times \mathbf{F}) \tag{E.9}$$

For convenience, the fields are expressed as the superposition of components transverse magnetic (TM) and transverse electric (TE) to r, that is, in terms of A_r and F_r. Letting $\mathbf{A} = \mathbf{u}_r A_r$ and $\mathbf{F} = \mathbf{u}_r F_r$ and expanding (E.8-E.9), the result is :

$$E_r = \frac{1}{j\omega\epsilon}\left(\frac{\partial^2}{\partial r^2} + k^2\right) A_r \tag{E.10}$$

$$E_\theta = \frac{-1}{r\sin\theta}\frac{\partial F_r}{\partial \phi} + \frac{1}{j\omega\epsilon r}\frac{\partial^2 A_r}{\partial r \partial \theta} \tag{E.11}$$

$$E_\phi = \frac{1}{r}\frac{\partial F_r}{\partial \phi} + \frac{1}{j\omega\epsilon r\sin\theta}\frac{\partial^2 A_r}{\partial r \partial \phi} \tag{E.12}$$

$$H_r = \frac{1}{j\omega\mu}\left(\frac{\partial^2}{\partial r^2} + k^2\right) F_r \tag{E.13}$$

$$H_\theta = \frac{1}{r\sin\theta}\frac{\partial A_r}{\partial \phi} + \frac{1}{j\omega\mu r}\frac{\partial^2 F_r}{\partial r \partial \theta} \tag{E.14}$$

$$H_\phi = -\frac{1}{r}\frac{\partial A_r}{\partial \theta} + \frac{1}{j\omega\mu r\sin\theta}\frac{\partial^2 F_r}{\partial r \partial \phi} \tag{E.15}$$

Appendix F

Wave Transformation

A transformation is determined to express a plane wave e^{jz} in terms of spherical wave functions [1]. The wave is finite at the origin and independent of ϕ, hence an expansion of the form

$$e^{jz} = e^{jr\cos\theta} = \sum_{n=0}^{\infty} a_n j_n(r) P_n(\cos\theta)$$

must be possible. To evaluate a_n, multiply each side by $P_q(\cos\theta)\sin\theta$ and integrate from 0 to π on θ. Because of orthogonality, all terms except $q = n$ vanish, and we get

$$\int_0^{\pi} e^{jr\cos\theta} P_n(\cos\theta)\sin\theta d\theta = \frac{2a_n}{2n+1} j_n(r)$$

The nth derivative of the left hand side with respect to r evaluated at $r = 0$ is

$$j^n \int_0^{\pi} \cos^n\theta P_n(\cos\theta)\sin\theta d\theta = \frac{j^n 2^{n+1}(n!)^2}{(2n+1)!}$$

[1] This derivation is largely reproduced from Harrington [19]

The nth derivative of the right hand side evaluated at $r = 0$ is

$$\frac{2^{n+1}(n!)^2}{(2n+1)(2n+1)!}a_n$$

Equating the preceding two expressions yields

$$a_n = j^n(2n+1)$$

which substituting back into the starting equation gives,

$$e^{jz} = e^{jr\cos\theta} = \sum_{n=0}^{\infty} j^n(2n+1)j_n(r)P_n(\cos\theta) \tag{F.1}$$

which is the desired transform. Note the following identity has also been established

$$j_n(r) = \frac{j^{-n}}{2}\int_0^{\pi} e^{jr\cos\theta}P_n(\cos\theta)\sin\theta d\theta$$

F.1 Incident Field

Assuming the incident electric field of a uniform plane wave is linearly polarised in the x direction and is travelling along the z axis. The electric field can be expressed as

$$\mathbf{E}^i = \hat{x}E_x^i = \hat{x}E_0e^{-jkz} = \hat{x}E_0e^{-jkr\cos\theta} \tag{F.2}$$

and transformed into spherical coordinates as

$$\mathbf{E}^i = \hat{r}E_r^i + \hat{\theta}E_\theta^i + \hat{\phi}E_\phi^i \tag{F.3}$$

where

$$\begin{aligned} E_r^i &= E_x^i \sin\theta\cos\phi \\ &= E_0 \sin\theta\cos\phi e^{-jkr\cos\theta} \qquad \text{(F.4)} \\ E_\theta^i &= E_x^i \cos\theta\cos\phi \\ &= E_0 \cos\theta\cos\phi e^{-jkr\cos\theta} \qquad \text{(F.5)} \\ E_\phi^i &= -E_x^i \cos\phi \\ &= -E_0 \cos\phi e^{-jkr\cos\theta} \qquad \text{(F.6)} \end{aligned}$$

The radial $\mathbf{E}^i$ component is given by

$$E_r^i = E_x^i \sin\theta\cos\phi = E_0 \frac{\cos\phi}{jkr}\frac{\partial}{\partial\theta} e^{-jkr\cos\theta} \qquad \text{(F.7)}$$

Using the wave transformation described in equation (F.1), the above equation can be written in terms of spherical wave functions as

$$E_r^i = E_0 \frac{\cos\phi}{jkr}\sum_{n=0}^{\infty} j^{-n}(2n+1) j_n(kr)\frac{\partial}{\partial\theta} P_n(\cos\theta) \qquad \text{(F.8)}$$

where $j_n(kr)$ is a spherical Bessel function of the first kind and $P_n(\cos\theta)$ is an ordinary Legendre function. The above equation can be simplified by replacing the $j_n(kr)$ with a *Schulkenov spherical Bessel function* which is related to ordinary spherical Bessel functions and spherical Bessel functions by

$$\hat{Z}_n(kr) = krz_n(kr) = \sqrt{\frac{\pi kr}{2}} Z_{n+1/2}(kr) \qquad \text{(F.9)}$$

Further simplification involves using the relation

$$\frac{\partial P_n(\cos\theta)}{\partial\theta} = P_n^1(\cos\theta) \qquad \text{(F.10)}$$

and noting that $n = 0$ falls away since $P_0^1 = 0$. The result is

$$E_r^i = -\frac{jE_0 \cos\phi}{(kr)^2} \sum_{n=1}^{\infty} j^{-n}(2n+1)\hat{J}_n(kr)P_n^1(\cos\theta) \tag{F.11}$$

The magnetic vector potential (which is similar in form to E_r^i) is constructed as

$$A_r^i = \frac{E_0}{\omega\mu} \cos\phi \sum_{n=1}^{\infty} a_n \hat{J}_n(kr)P_n^1(\cos\theta) \tag{F.12}$$

and E_r^i can be evaluated using equation (E.10) to yield

$$E_r^i = -\frac{jE_0 \cos\phi}{(kr)^2} \sum_{n=1}^{\infty} a_n n(n+1)\hat{J}_n(kr)P_n^1(\cos\theta) \tag{F.13}$$

Equating this with equation (F.11) reveals that

$$a_n = \frac{j^{-n}(2n+1)}{n(n+1)} \tag{F.14}$$

Similarly, H_r^i can be produced from

$$F_r^i = \frac{E_0}{k} \sin\phi \sum_{n=1}^{\infty} a_n \hat{J}_n(kr)P_n^1(\cos\theta) \tag{F.15}$$

F.2 Scattered Field

The scattered field will be generated by an A_r and F_r of the same form as the incident field with J_n replaced by Schulkenov spherical Hankel functions of the second kind [2], $\hat{H}_n^{(2)}$, to represent outwardly travelling waves (see appendix E.1). Hence scattered potentials are

[2] These are related to ordinary Hankel functions by equation (F.9)

constructed as

$$A_r^s = \frac{E_0}{\omega\mu}\cos\phi\sum_{n=1}^{\infty} b_n \hat{H}_n^{(2)}(kr)P_n^1(\cos\theta) \tag{F.16}$$
$$F_r^s = \frac{E_0}{k}\sin\phi\sum_{n=1}^{\infty} c_n \hat{H}_n^{(2)}(kr)P_n^1(\cos\theta)$$

The total field is simply the superposition of the incident and scattered fields. The **E** and **H** fields can therefore be determined from equations (E.10-E.15) where

$$A_r = A_r^i + A_r^s = \frac{E_0}{\omega\mu}\cos\phi\sum_{n=1}^{\infty}[a_n\hat{J}_n(kr) + b_n\hat{H}_n^{(2)}(kr)]P_n^1(\cos\theta) \tag{F.17}$$
$$F_r = F_r^i + F_r^s = \frac{E_0}{k}\sin\phi\sum_{n=1}^{\infty}[a_n\hat{J}_n(kr) + c_n\hat{H}_n^{(2)}(kr)]P_n^1(\cos\theta)$$

Boundary conditions need to be enforced on the circumference of the sphere and will determine the values of b_n and c_n.

Evaluation of the **E** and **H** fields involves substitution of A_r^s and F_r^s, in equations (F.16), into the field solutions of equations (E.10-E.15). The scattered electric field components specifically can be expressed in this way as

$$E_r^s = -jE_0\cos\phi\sum_{n=1}^{\infty} b_n\left[\hat{H}_n''^{(2)}(kr) + \hat{H}_n^{(2)}(kr)\right]P_n^1(\cos\theta) \tag{F.18}$$
$$E_\theta^s = \frac{E_0}{kr}\cos\phi\sum_{n=1}^{\infty}\left[jb_n\hat{H}_n'^{(2)}(kr)\sin\theta P_n'^1(\cos\theta) - c_n\hat{H}_n^{(2)}(kr)\frac{P_n^1(\cos\theta)}{\sin\theta}\right] \tag{F.19}$$
$$E_\phi^s = \frac{E_0}{kr}\sin\phi\sum_{n=1}^{\infty}\left[jb_n\hat{H}_n'^{(2)}(kr)\frac{P_n^1(\cos\theta)}{\sin\theta} - c_n\hat{H}_n^{(2)}(kr)P_n'^1(\cos\theta)\right] \tag{F.20}$$

where

$$\hat{H}_n'^{(2)}(x) = \frac{\partial\hat{H}_n^{(2)}(x)}{\partial x} \qquad \hat{H}_n''^{(2)}(x) = \frac{\partial^2\hat{H}_n^{(2)}(x)}{\partial x^2} \qquad P_n'^1(u) = \frac{\partial P_n^1(u)}{\partial u}$$

and can be determined from the recursion formulas

$$\frac{\partial \hat{H}_n^{(2)}(kr)}{\partial(kr)} = -nh_n^{(2)}(kr) + krh_{n-1}^{(2)}(kr) \tag{F.21}$$

$$\frac{\partial^2 \hat{H}_n^{(2)}(kr)}{\partial(kr)^2} = \left(\frac{n(n+1)}{2n+1}\right) h_{n+1}^{(2)}(kr) - \left(\frac{3n^2-n-1}{2n+1}\right) h_{n-1}^{(2)}(kr) + krh_{n-2}^{(2)}(kr) \tag{F.22}$$

Appendix G

Rough Surface Generation MATLAB Code

```
% RMS surface height
h = 0.159;
% Correlation length
l = 0.675;
% Spatial discretization
dx = 1/5;
% Number of surface points
N = 1024;
% surface points
x = [1:N] * dx;
% Total length
L = N*dx;
% Spatial wavenumber
Jp = [0:N/2-1];
Kp = 2 * pi * Jp / L;
```

```
% Determine F(K_j)
for m = 1:N/2+1
  Fp(m) = FTrfm(Kp(m),Jp(m),L,l,h,N);
end;
% Conjugate symmetry
Fm = fliplr(conj(Fp));
% Piece the positive and negative halves together
Fm(N/2+1) = [];
Fp(N/2+1) = [];
F = [Fm Fp];

% Perform the inverse FFT
f = ifft(fftshift(F),N);
% The result is normalised with respect to the discretisation
f = real(f)/dx;

% ====================
% Function that determines F(K_j)
function [F] = FTrfm(K,J,L,l,h,N)
% Normalised Gaussian spectrum
W = exp( -(K.*l/2).^2) .* (l.*h.^2) / (2*sqrt(pi));
term1 = sqrt( 2 * pi * L * W );
% fortunately Matlab has a built in Gaussian number generator.
if (J==0)|(J==N/2)
  F = term1 * randn;
  return;
else
  F = term1 * (randn + i*randn) / sqrt(2);
  return;
end;
```